



Title	Diurnal Variations in Lower-Tropospheric Wind over Japan Part II: Analysis of Japan Meteorological Agency Mesoscale Analysis Data and Four Global Reanalysis Data Sets
Author(s)	Sakazaki, Takatoshi; Fujiwara, Masatomo
Citation	Journal of the Meteorological Society of Japan, 88(3), 349-372 <a href="https://doi.org/10.2151/jmsj.2010-306">https://doi.org/10.2151/jmsj.2010-306</a>
Issue Date	2010-07-21
Doc URL	<a href="http://hdl.handle.net/2115/44057">http://hdl.handle.net/2115/44057</a>
Type	article
File Information	JMSJ88-3_349-372.pdf



[Instructions for use](#)

## Diurnal Variations in Lower-Tropospheric Wind over Japan Part II: Analysis of Japan Meteorological Agency Mesoscale Analysis Data and Four Global Reanalysis Data Sets

Takatoshi SAKAZAKI and Masatomo FUJIWARA

*Graduate School of Environmental Science, Hokkaido University, Sapporo, Japan*

*(Manuscript received 24 November 2009, in final form 19 February 2010)*

### Abstract

Following on from the observation results obtained from Wind profiler Network and Data Acquisition System (WINDAS) data, as reported by Part I of this study, the dynamical processes responsible for the diurnal component in lower-tropospheric winds are examined using Japan Meteorological Agency (JMA) mesoscale analysis data (MANAL) and four global reanalysis data sets (JRA25/JCDAS, ERA-Interim, NCEP1, and NCEP2). Of these data sets, MANAL and JRA25 perform best in reproducing the WINDAS horizontal wind observations, including their diurnal and semidiurnal components. At 1–3 km height, Diurnal Eastward-moving Eddies (DEEs) with a phase speed of 10–15 m s<sup>-1</sup> and diameter of ~700 km move eastward over the Sea of Japan and over the Pacific throughout the year. The superposition of winds associated with DEEs over return currents controls the diurnal wind component over the main Japanese islands, generating diurnal amplitude maxima in spring and autumn at this height range. Analysis of global reanalysis data confirmed that the diurnal wind at 3–5 km in winter–spring is controlled mainly by medium-scale eastward-traveling waves with amplitude maxima around the tropopause. The diurnal wind at 3–5 km in summer–autumn is caused primarily by the diurnal tide with zonal wavenumbers of ≤10. For stations located on small islands south of the Japanese mainland, the diurnal wind is controlled mainly by the diurnal tide for the entire lower troposphere throughout the year.

### 1. Introduction

In a companion paper, Sakazaki and Fujiwara (2010; hereafter referred to as SF10) investigated diurnal variations in lower tropospheric wind over Japan, using a 6-year data set obtained by the Wind profiler Network and Data Acquisition System (WINDAS) in Japan. The authors examined the characteristics of diurnal and semidiurnal components of zonal wind ( $u$ ) and meridional wind ( $v$ ) for each height range and for each season. SF10 attributed the semidiurnal component to an atmospheric semidiurnal migrating tide above ~1 km and to local wind systems below ~1 km, through-

out the year. In addition, the lower tropospheric semidiurnal tide shows a seasonal variation, with a maximum amplitude in winter. In contrast, the characteristics of the diurnal wind component are strongly dependent on location (the main Japanese islands or small southern islands; see Fig. 1 of SF10), height (near the surface, 1–3 km, or 3–5 km), and season. Near the surface of the main Japanese islands, local wind systems (mainly land–sea breezes) are dominant throughout the year, with maximum amplitudes from spring to autumn. At 1–3 km height, the return currents of the local wind systems are observed throughout the year. At this height range, the amplitude attains maxima in spring and autumn. The spring maximum is observed for stations along the north coast of the main Japanese islands, while the autumn maximum is observed at stations along the south coast. Considering that local wind systems are strongest in summer (in terms

---

Corresponding author: Takatoshi Sakazaki, Graduate School of Environmental Science, Hokkaido University, Sapporo, Hokkaido 060-0810, Japan.  
E-mail: zaki@ees.hokudai.ac.jp  
© 2010, Meteorological Society of Japan

of surface winds), SF10 inferred that these spring/autumn maxima are caused by the superposition of larger-scale disturbances on the return currents. These disturbances show an eastward phase propagation in winter–spring at 34–40°N and the zonal phase speed is estimated to be  $\sim 20 \text{ m s}^{-1}$ . Above  $\sim 3 \text{ km}$ , the amplitudes attain a maximum in February, and the amplitudes of  $v$  are larger than those of  $u$ . In this height region, in winter–spring, the phase propagates eastward at  $\sim 35^\circ\text{N}$ . The zonal phase speed is estimated to be  $\sim 25 \text{ m s}^{-1}$ , faster than that of the disturbance at 1–3 km. SF10 suggested that medium-scale eastward-traveling waves centered in the upper troposphere control the diurnal wind component, resulting in the amplitude maximum in February. In summer–autumn, in contrast, the phases of most stations are coherent, suggesting that a much larger-scale wind system prevails, with a horizontal scale of  $>3000 \text{ km}$ . This wind system may be due to the atmospheric diurnal tide, although the phase is not consistent with that in a tidal model (GSWM02). Finally, it was found that the diurnal component at stations on small southern islands shows different characteristics to that recorded at stations upon the main Japanese islands.

In this paper, we investigate the four dynamical processes that contribute to the observed characteristics in the diurnal wind component over Japan; these processes are (1) the eastward-moving disturbance at 1–3 km in winter–spring, (2) the eastward-traveling disturbance at 3–5 km in winter–spring, (3) the large-scale ( $>3000 \text{ km}$ ) wind system at 3–5 km in summer–autumn, and (4) the wind system over the small southern islands throughout the entire lower troposphere. Since 2001, the Japan Meteorological Agency (JMA) has been operating the meso-scale analysis (MANAL), which is used as the initial conditions for the JMA Meso-Scale Model (MSM). The analysis covers the region of 120–150°E and 22–46°N (Fig. 1), and is performed every 3 or 6 hours with a fine horizontal resolution ( $\sim 11 \times 11 \text{ km}$  or  $\sim 22 \times 22 \text{ km}$ ). This data set should be appropriate for examining the nature of diurnal wind variations over Japan, particularly for local–mesoscale phenomena. Furthermore, four-times-daily global reanalysis data, which cover the entire globe, are used to investigate the global structure of the diurnal wind component.

We first examine the validity of wind data, including their diurnal and semidiurnal components,

in the lower troposphere in the above analysis data sets by comparing them with WINDAS observations. Subsequently, we investigate the four dynamical processes mentioned above. The remainder of this paper is organized as follows. Section 2 describes the data sets and analysis methods, and in Section 3 we examine the validity of horizontal winds in the analysis data sets, including their diurnal and semidiurnal components. In Section 4, we investigate the diurnal component, considering the return currents, diurnal eastward-moving eddies (DEEs), atmospheric tides, and medium-scale eastward-traveling waves. Finally, the main findings are summarized in Section 5.

## 2. Data and analysis methods

We use MANAL data for the 5-year period from April 2003 to March 2008 (1 year shorter than the analysis period for WINDAS/AMeDAS data considered in SF10). Data are available every 3 hours. Note that for the period prior to February 2006, assimilated values are obtained only four times daily, at 0000, 0600, 1200, and 1800 UTC, while the data at 0300, 0900, 1500, and 2100 UTC are predicted using the model. After February 2006, the data consist only of assimilated data every 3 hours. In this study, we analyze assimilated data only. In MANAL, the wind data from WINDAS are assimilated with an assimilation window of 3 hours (6 hours) before (after) February 2006, using a four-dimensional variational method. Several physical schemes in the model and the dynamical core have changed several times during the analysis period (JMA Numerical Prediction Division 2008). Detailed information regarding MANAL can be found in JMA Numerical Prediction Division (2008).

Figure 1 shows the region covered by MANAL, as well as the locations of WINDAS stations. The stations are located on the four main islands of Japan (hereafter referred to as the main Japanese islands) and small islands located south of the Japanese mainland (small southern islands) (see Fig. 1 in SF10). Central Honshu is dominated by mountainous areas ( $\sim 2000 \text{ m}$  above sea level); the MANAL model treats topographical features better than does reanalysis. The horizontal spacing of MANAL is  $0.25^\circ \times 0.2^\circ$  ( $\sim 22 \times 22 \text{ km}$  at  $35^\circ\text{N}$ ) for the period before February 2006, and  $0.125^\circ \times 0.1^\circ$  ( $\sim 11 \times 11 \text{ km}$  at  $35^\circ\text{N}$ ) after February 2006. The vertical levels of output data are 1000 (only after February 2006), 975, 950, 925,

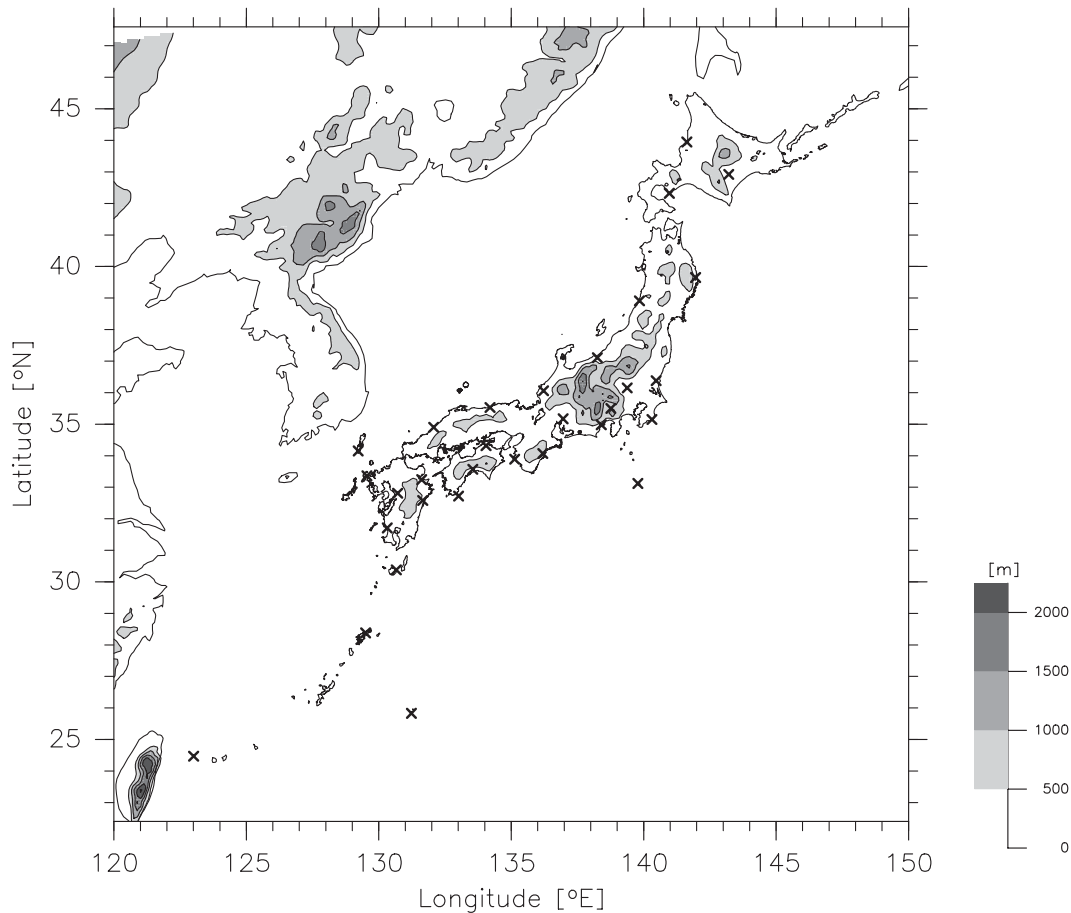


Fig. 1. Extent of the region considered in MANAL. WINDAS stations are denoted by crosses. Contour lines show the coast and topography at intervals of 500 m. At 35°N, 1° of longitude corresponds to ~90 km.

900, 850, 800, 700, 600 (only after February 2006), 500, 400, 300, 250, 200, 150, and 100 hPa. Of these levels, those used in the present study are summarized in Table 1.

We also use the following four global reanalysis data sets for examining the global structures of diurnal wind variations: NCEP/NCAR reanalysis data (NCEP1) (Kalnay et al. 1996), NCEP-DEO AMIP-II reanalysis data (NCEP2) (Kanamitsu et al. 2002), ECMWF reanalysis data (ERA-Interim) (Simmons et al. 2006; Uppala et al. 2008), and Japanese reanalysis data (JRA25/JCDAS; hereafter referred to as JRA25) (Onogi et al. 2007). These data sets are all four-times daily, at 0000, 0600, 1200, and 1800 UTC. We analyze data for a 6-year period from April 2002 to March 2008 (the same period as that considered in SF10). The horizontal spacing of the data is  $2.5^\circ \times 2.5^\circ$  for NCEP1 and NCEP2,  $1.5^\circ \times 1.5^\circ$  for ERA-Interim,

and  $1.25^\circ \times 1.25^\circ$  for JRA25. The number of pressure levels is 17 for NCEP1 and NCEP2, 37 for ERA-Interim, and 23 for JRA25. The top level is 10 hPa for NCEP1 and NCEP2, 1 hPa for ERA-Interim, and 0.4 hPa for JRA25. Of these vertical levels, the levels used in this study are listed in Table 1. It should be noted that the WINDAS observations are assimilated in JRA25 and ERA-Interim, but not in NCEP1 and NCEP2.

The procedures employed in data processing and analysis are basically the same as those for WINDAS and AMeDAS data in SF10, as briefly explained below. By performing a 3-month running average for each pressure level and each local time, 3-hourly (for MANAL data) and 6-hourly (for MANAL and global reanalysis data) composite data are calculated for each grid point, for each pressure level, and for each month. Because of the change in the temporal and spatial resolution of

Table 1. Pressure levels of MANAL and reanalysis data that roughly correspond to the height levels of WINDAS observations. The pressure levels in MANAL/global reanalysis are denoted by  $\circ$ . For MANAL, the pressure levels present only in MANAL2 are denoted by  $\triangle$ .

WINDAS height (km)	0.4	0.7	1.0	1.3	1.6	1.9	2.2	2.5	3.1	3.6	4.2	4.8	5.1
Pressure level (hPa)	975	925	900	875	850	800	775	750	700	650	600	550	500
MANAL	$\circ$	$\circ$	$\circ$	—	$\circ$	$\circ$	—	—	$\circ$	—	$\triangle$	—	$\circ$
JRA25/JCDAS	—	$\circ$	—	—	$\circ$	—	—	—	$\circ$	—	$\circ$	—	$\circ$
ERA-Interim	$\circ$	$\circ$	$\circ$										
NCEP1	—	$\circ$	—	—	$\circ$	—	—	—	$\circ$	—	$\circ$	—	$\circ$
NCEP2	—	$\circ$	—	—	$\circ$	—	—	—	$\circ$	—	$\circ$	—	$\circ$

MANAL data (as described above), two kinds of composite data are prepared for MANAL data: one obtained using the assimilated values every 6 hours for the entire 5 years using grid points of  $0.25^\circ \times 0.2^\circ$  in size (denoted as MANAL1), and the other obtained using the assimilated values every 3 hours, only for the last 2 years, using grid points of  $0.125^\circ \times 0.1^\circ$  in size (denoted as MANAL2). For MANAL2, the diurnal and semi-diurnal components are extracted by Fourier analysis. For MANAL1 and all of the reanalysis, only the diurnal component is extracted. The 3-hourly data used in Figs. 10–13 and 16–17 are compiled using this harmonic diurnal component.

For global reanalysis data, we represent the spatial and temporal dependence of the diurnal component of  $u$  and  $v$  as

$$X(\lambda, \phi, z, t) = \sum_{s=-n}^n [a_s(\phi, z) \cos(\omega t + s\lambda) + b_s(\phi, z) \sin(\omega t + s\lambda)], \quad (1)$$

following the method by Haurwitz and Cowley (1973). Here,  $X$  is either  $u$  or  $v$ ;  $\lambda$ ,  $\phi$ , and  $z$  are longitude, latitude, and altitude, respectively;  $t$  is time in Universal Time (UT);  $n$  is half the total number of grid points in longitude;  $a_s$  and  $b_s$  are harmonic amplitudes;  $\omega$  is the angular velocity of the Earth's rotation; and  $s$  is the zonal wavenumber. The sign of  $s$  represents the direction of wave propagation, with positive values for westward-propagating disturbances.

### 3. Validation of analysis and reanalysis data

Here, we validate the winds in MANAL and global reanalysis data by comparing them with WINDAS winds. In Section 3.1, we validate the

original winds (i.e., the wind data before performing composite analysis). In Sections 3.2 and 3.3, the diurnal and semidiurnal components of the original winds are validated, respectively. The correspondence between height levels in WINDAS data and pressure levels in analysis data follows that shown in Table 1.

#### 3.1 Validation of original winds

Following Willmott (1982), we calculate the intercept,  $a$ , and slope,  $b$ , of the least-squares regression,  $P_i = a + bO_i$ , where  $O_i$  is a WINDAS value and  $P_i$  is a MANAL/global reanalysis value at the grid point closest to each WINDAS station. Least-mean-square errors (RMSEs) and the index of agreement,  $d$ , are also calculated.  $d$  is defined as

$$d = 1 - \left[ \frac{\sum_{i=1}^N (P_i - O_i)^2}{\sum_{i=1}^N (|P_i - \bar{O}| + |O_i - \bar{O}|)^2} \right], \quad (2)$$

where  $\bar{O}$  represents the average of  $O_i$ , and  $N$  is the number of data used for the calculation. The denominator of the second term in Eq. (2) can be viewed as a measure of the sum of variance, whereas the numerator is the sum of square errors. Thus, the second term is roughly regarded as the ratio of errors to the variance. This index varies from 0.0 (i.e., no agreement between  $P_i$  and  $O_i$ ) to 1.0 (i.e., perfect agreement) (for details, see Willmott 1982). The index is widely used for model validation to assess the reproducibility of observation results (e.g., Cai and Steyn 2000; Nitis et al. 2005).

Figure 2 shows vertical profiles of  $a$ ,  $b$ , RMSE, and  $d$  for zonal and meridional winds in DJF and

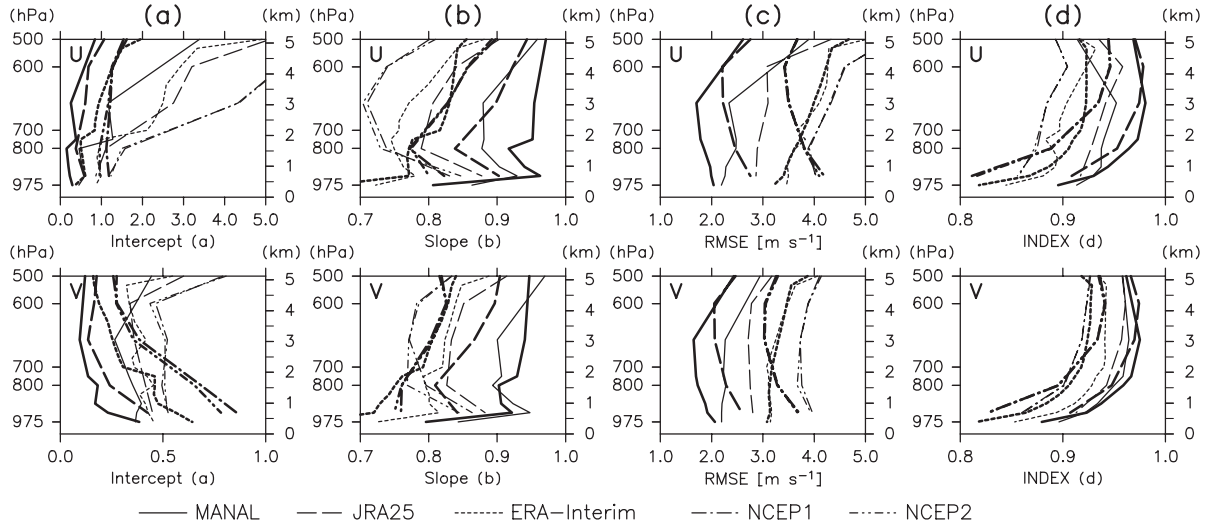


Fig. 2. Vertical profiles of the (a) intercept and (b) slope of the least-squares regression, (c) RMSE, and (d) index of agreement, for (top) the zonal wind component and (bottom) the meridional wind component, with respect to WINDAS data. Solid lines are for MANAL1, dashed lines for JRA25, dotted lines for ERA-Interim, dot-dashed lines for NCEP1, and dot-dot-dashed lines for NCEP2. Thick (thin) lines are for JJA (DJF). The correspondence between pressure levels and height levels follows that described in Table 1. See the text for details.

JJA. This figure shows a number of features. First, all data sets show that  $a$  (Fig. 2a) is positive for both zonal and meridional winds throughout the year, and is larger for  $u$  than for  $v$  (note the difference in the abscissa range between  $u$  and  $v$ ). In addition,  $a$  in DJF is larger than that in JJA. Second,  $b$  (Fig. 2b) is approximately constant with height (0.75–0.95), except near the surface, and  $b$  in DJF is generally smaller than that in JJA. Third, RMSE (Fig. 2c) is near-constant with height. RMSE in DJF is larger than that in JJA for all data sets; the reproducibility is relatively poor in DJF. Finally,  $d$  (Fig. 2d) is small below  $\sim 1$  km, but is nearly constant with height above  $\sim 1$  km, yielding values close to one for both  $u$  and  $v$  throughout the year. There is no marked difference in  $d$  between zonal and meridional winds or between DJF and JJA.

Among the data sets, MANAL performs best in reproducing the WINDAS winds: for both  $u$  and  $v$ ,  $a$  is smallest,  $b$  is closest to unity, RMSE is smallest, and  $d$  is closest to unity. Of the four global reanalysis data sets, reproducibility is best for JRA25; the other three data sets show similar performance in terms of lower-tropospheric winds over Japan. The difference between NCEP1 and NCEP2 is so small that the corresponding trend lines (Fig. 2) largely overlap.

### 3.2 Validation of the diurnal wind component

The diurnal component in WINDAS is obtained from hourly hourly-averaged data (as explained in SF10), while that in MANAL1 and reanalysis is from 6-hourly snapshot data. The following results do not change if we use only 6-hourly hourly-averaged WINDAS data (not hourly data) in calculating the diurnal component. This finding indicates that negligible error arises from the difference in sampling interval. In Section 3.2.a, we examine the average errors in these data sets, and in Section 3.2.b we validate the horizontal inhomogeneity of the diurnal wind component over Japan. In Section 3.2.c, the seasonality is validated.

#### a. Root-mean-square errors

Figure 3 shows vertical profiles of RMSE for the amplitude (RMSEa), phase (RMSEp), and harmonic dial vector (RMSEh) of the diurnal wind component for  $u$  and  $v$ . The harmonic dial vectors represent the amplitude and phase of any harmonic component based on their length and direction, respectively. RMSEh is defined as

$$\text{RMSEh} = \sqrt{\frac{1}{N_p} \sum_{i=1}^{N_p} |V_W - V_A|^2}, \quad (3)$$

where  $V_W$  and  $V_A$  are the harmonic dial vectors

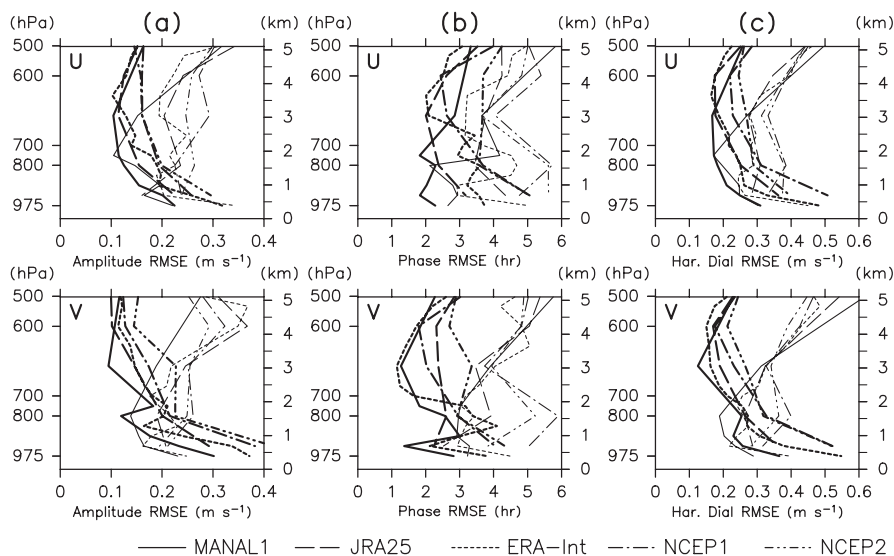


Fig. 3. As for Fig. 2, but for RMSE for the diurnal wind component in terms of the (a) amplitude, (b) phase, and (c) harmonic dial vector. See the text for details.

of the WINDAS and analyses, respectively, and  $N_p$  is the total number of WINDAS stations. By definition, RMSEh is related to both RMSEa and RMSEp. As in Section 3.1, the analysis data at the horizontal and vertical grid points closest to each WINDAS station are used for calculation. In Fig. 3a, RMSEa in DJF is nearly constant at 0.2–0.3  $\text{m s}^{-1}$ . In JJA, RMSEa attains a maximum of 0.3–0.4  $\text{m s}^{-1}$  near the surface but shows a constant value at 0.1–0.2  $\text{m s}^{-1}$  with increasing height above  $\sim 1$  km. Considering the diurnal amplitudes of WINDAS data (Fig. 7 in SF10), the relative ratio of errors is  $\sim 0.5$  near the surface in both DJF and JJA, and  $\sim 0.4$  ( $< 0.2$ ) in DJF (JJA) above  $\sim 1$  km. In DJF (JJA), RMSEp is constant at 3–5 hr (2–4 hr) (Fig. 3b), corresponding to just  $\sim \pi/6$  ( $\sim \pi/8$ ) radians in DJF (JJA). In Fig. 3c, RMSEh summarizes the findings for RMSEa and RMSEb. RMSEh is 0.3–0.4 (0.2–0.3)  $\text{m s}^{-1}$  in DJF (JJA), except for large values near the surface. Thus, the diurnal wind component in WINDAS is reproduced reasonably well, particularly above  $\sim 1$  km and in JJA. The reproducibility is best for

MANAL1, followed by JRA25 and ERA-Interim.

#### b. Spatial inhomogeneity

In addition to the above quantitative measures averaged over Japan, it is important to assess the reproducibility of the spatial characteristics of the diurnal wind component observed by WINDAS. Figure 4 shows the harmonic dial vectors of the MANAL1/JRA25 diurnal component of  $v$  at 1.6 km (850 hPa) and 5.1 km (500 hPa) in DJF and JJA.

The key findings in SF10 regarding WINDAS winds at 1–3 km, including the 850 hPa level, are an eastward phase propagation in DJF–MAM and a phase contrast between the north and south coasts of the main Japanese islands associated with the return currents of the surface wind system throughout most of the year. For phase propagation, at 850 hPa in DJF (Figs. 4a, e), the WINDAS phase for stations at  $\sim 35^\circ\text{N}$  shows that the phase is  $\sim 0700$  LT at  $130^\circ\text{E}$ ,  $\sim 1300$  LT at  $135^\circ\text{E}$ , and  $\sim 1800$  LT at  $140^\circ\text{E}$ , indicating an eastward-propagating disturbance. The MANAL1

Fig. 4. Harmonic dial vectors of the diurnal component of  $v$ . Thick arrows represent vectors derived from WINDAS data, while thin vectors represent vectors derived from (a–d) MANAL1 and (e–h) JRA25 data. (a) and (e) are for 850 hPa (1.6 km) in DJF, (b) and (f) are for 850 hPa (1.6 km) in JJA, (c) and (g) are for 500 hPa (5.1 km) in DJF, and (d) and (h) are for 500 hPa (5.1 km) in JJA, in MANAL1/JRA25 (WINDAS). Reference harmonic dial vectors are shown at bottom right.

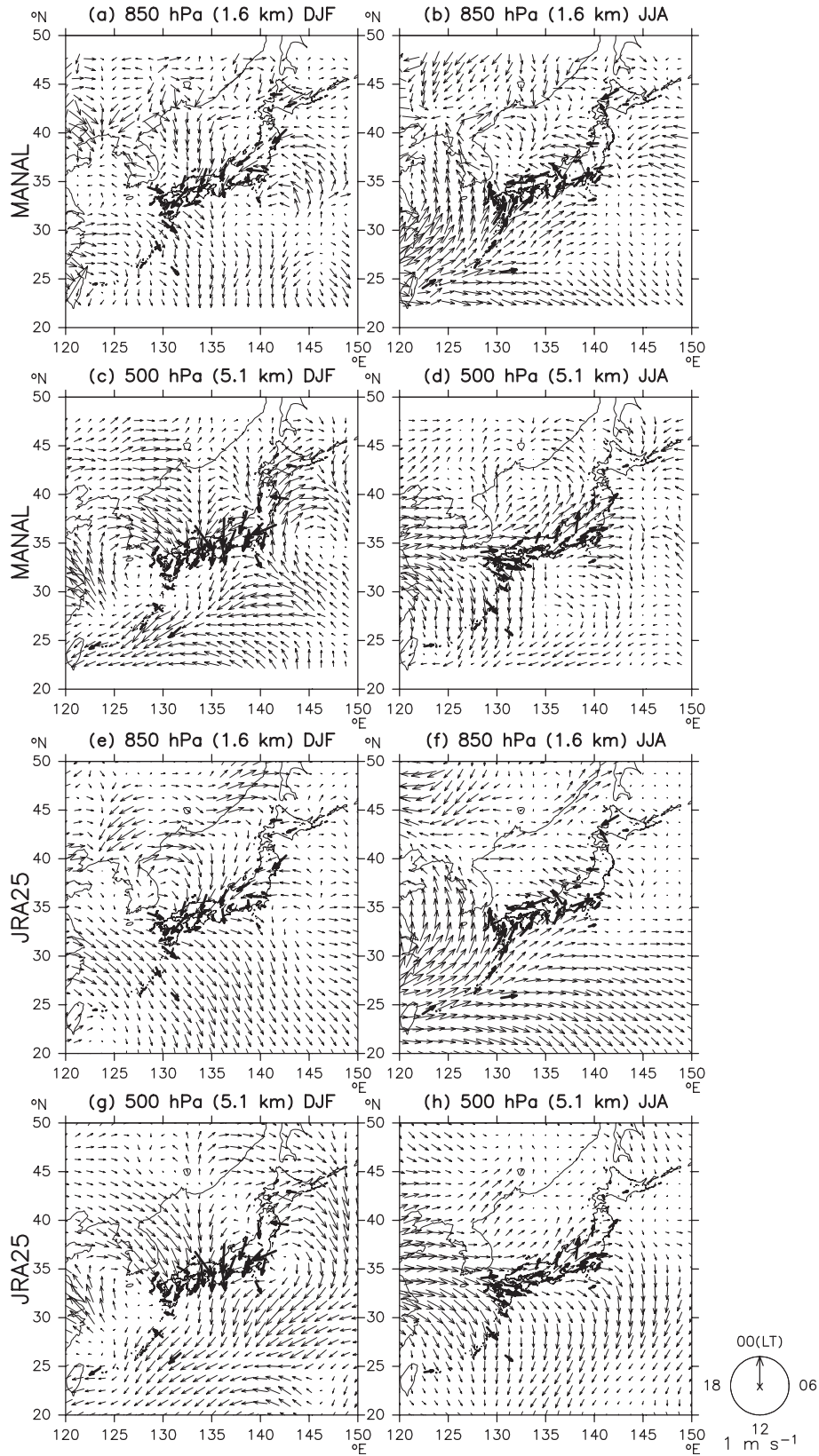


(Fig. 4a) and JRA25 (Fig. 4e) vectors are largely consistent with this phase propagation, showing that the phase at 35–40°N is ~0600 LT at 130°E, ~1200 LT at 135°E, and ~1800 LT at 140°E. For the phase contrast due to the return currents, at 850 hPa in JJA (Figs. 4b, f), the WINDAS phase for stations along the north (south) coast of the main Japanese islands is ~1800 LT (~0300 LT); that is, the winds are onshore during the nighttime. This phase contrast is also well reproduced by MANAL1 (Fig. 4b) and JRA25 (Fig. 4f).

The key findings in SF10 regarding WINDAS winds at 3–5 km, including the 500 hPa level, are an eastward phase propagation in DJF–MAM and coherent phases over Japan in JJA–SON. For phase propagation, at 500 hPa in DJF (Figs. 4c, g), the WINDAS vectors for stations at ~35°N show that the phase is ~0700 LT at 132°E, ~1300 LT at 135°E, and ~1700 LT at 140°E, indicating an eastward-propagating disturbance. This phase propagation is well reproduced by both MANAL1 (Fig. 4c) and JRA25 (Fig. 4g), although the phases in MANAL1/JRA25 are ~3 hr later than those in WINDAS, and the amplitudes in MANAL1/JRA25 are 0.2–0.4 m s<sup>-1</sup>, approximately half those in WINDAS (this trend is especially pronounced in eastern Japan). These errors result in the relatively large RMSEs in DJF, as shown in Fig. 3. For the coherent phases over Japan at 500 hPa in JJA (Figs. 4d, h), the WINDAS phases are almost constantly 0300–0900 LT, with amplitudes of ~0.5 m s<sup>-1</sup>; MANAL1 and JRA25 amplitudes and phases are consistent with these WINDAS values.

SF10 also reported that stations on small southern islands are influenced by a different wind system from that over the main Japanese islands throughout the entire lower troposphere during the whole year. At 850 hPa (Figs. 4a, b, e, f) for the region of (20–32°N, 120–135°E), the MANAL1 and JRA25 amplitudes are ~0.5 m s<sup>-1</sup> in both DJF and JJA, and the phases are coherent at 0900–1200 LT in DJF and at 0300–0600 LT in JJA. At 500 hPa (Figs. 4c, d, g, h), the MANAL1 and JRA25 amplitudes are ~0.5 m s<sup>-1</sup> in both DJF and JJA, and the phases are coherent at 0300–0700 LT in DJF and at 0900–1200 LT in JJA. These amplitudes and phases are largely consistent with those at WINDAS stations located on small southern islands. In addition, the MANAL1 and JRA25 vectors confirm that the wind system around these stations has a large horizontal scale

(>3000 km) at both 850 and 500 hPa and in both DJF and JJA, being different from that recorded by stations on the main Japanese islands.

The spatial inhomogeneity of the diurnal component of  $u$  is also examined (data not shown). In both MANAL1 and JRA25, the eastward phase delay is not seen at 850 hPa in DJF. At 500 hPa in DJF, the eastward phase propagation is observed only along the latitude region of ~40°N. In other areas at 500 hPa in DJF, the phases are different between the north and south coasts of the main Japanese islands. At 500 hPa in JJA, the winds are coherent over Japan. These features are consistent with the WINDAS observations reported in SF10.

Other global reanalysis data (ERA-Interim, NCEP1, NCEP2) give similar results to those derived from JRA25. Note that the eastward phase propagation at lower levels (~850 hPa) in DJF (Fig. 4a or e) is reproduced in the  $v$  of ERA-Interim at 850–700 hPa in winter–spring, but not by NCEP1 or NCEP2. This finding probably reflects the fact that WINDAS data are not assimilated in NCEP1 and NCEP2. The phase propagation at upper levels (~500 hPa) in DJF (Fig. 4c or g) is well reproduced by all the reanalysis data sets.

### c. Seasonal variations

Finally, we consider seasonal variations in the diurnal wind component. SF10 showed that the amplitudes near the surface are largest (~0.8 m s<sup>-1</sup>) in summer; those at 1–3 km show maxima in spring (~0.5 m s<sup>-1</sup>) and autumn (~0.6 m s<sup>-1</sup>), and those above 3 km show a maximum (~0.8 m s<sup>-1</sup>) in February. Figure 5 shows the month–pressure distributions of MANAL1 diurnal amplitudes averaged for the 31 grid points closest to each WINDAS station. Near the surface, the MANAL1 amplitude has a broad peak of 0.6–0.8 m s<sup>-1</sup> from spring to autumn for both  $u$  and  $v$ , consistent with the findings of SF10. At 850–700 hPa, the MANAL1 amplitude of  $u$  and  $v$  has a maximum of 0.4–0.5 m s<sup>-1</sup> in August–October, corresponding to the autumn maximum in WINDAS at 1–3 km, although the amplitude is ~0.2 m s<sup>-1</sup> smaller than that in WINDAS. Note that the spring maximum at 1–3 km in WINDAS is not reproduced in the all-station average in Fig. 5; however, it appears in the average for stations along the north coast (see Fig. 9a). Above 700 hPa, the MANAL1 amplitude reaches a maximum of ~0.4 m s<sup>-1</sup> in May for both  $u$  and  $v$ , with the amplitude of  $v$  being somewhat larger than that for  $u$ .

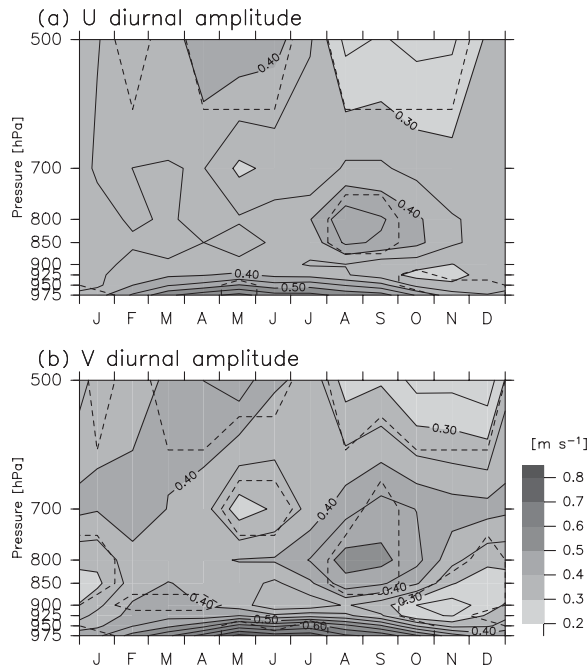


Fig. 5. Month–height distributions of the diurnal amplitudes of (a)  $u$  and (b)  $v$  derived from MANAL1 data, averaged for the 31 MANAL1 grid points closest to each WINDAS station. Dashed lines represent statistically significant regions (95% level;  $t$ -test).

This maximum corresponds to the February maximum in WINDAS, but the amplitude is approximately half that in WINDAS (SF10).

JRA25 and ERA-Interim data show a similar seasonal variation to that in MANAL, although the surface amplitude ( $0.4\text{--}0.5\text{ m s}^{-1}$ ) is smaller than that in WINDAS and MANAL1 ( $\sim 0.8\text{ m s}^{-1}$ ). In NCEP1 and NCEP2, the seasonal variation above 700 hPa is similar to that in MANAL1 (maximum in May), but the seasonal variation near the surface and at 850–700 hPa in WINDAS and MANAL1 is not reproduced.

### 3.3 Validation of the semidiurnal wind component

Here, we validate the semidiurnal wind component in MANAL2. The semidiurnal component in WINDAS is obtained from hourly hourly-averaged data, while the component in MANAL2 is derived from 3-hourly snapshot data. By comparing the results with those from only 3-hourly hourly-averaged WINDAS data, we confirmed the existence of negligible errors due to the difference in sampling interval. SF10 found that the semidiurnal phase of  $u$  ( $v$ ) is  $\sim 0400$  LT ( $\sim 0100$  LT) above 1 km; in addition, the semidiurnal amplitude is largely constant with height, and the amplitude is largest in winter ( $0.4\text{--}0.5\text{ m s}^{-1}$ ) and smallest in summer ( $0.2\text{--}0.3\text{ m s}^{-1}$ ).

Figure 6 shows vertical profiles of RMSEa, RMSEp, and RMSEh of the semidiurnal component for WINDAS and MANAL2. RMSEa is  $0.1\text{--}0.2\text{ m s}^{-1}$  and the relative ratio of errors is  $\sim 0.3$ . RMSEp is 1–2 hr, corresponding to  $\pi/12\text{--}$

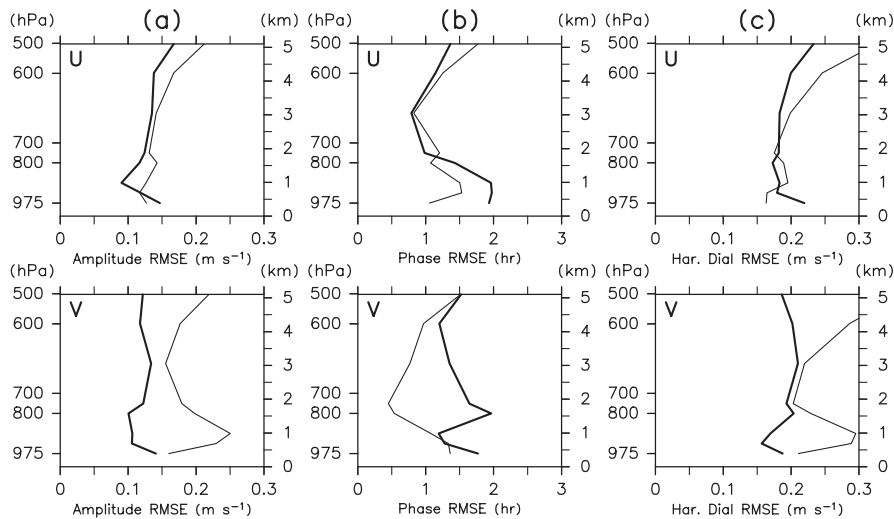


Fig. 6. As for Fig. 3, but for RMSE for the semidiurnal wind component between WINDAS and MANAL2.

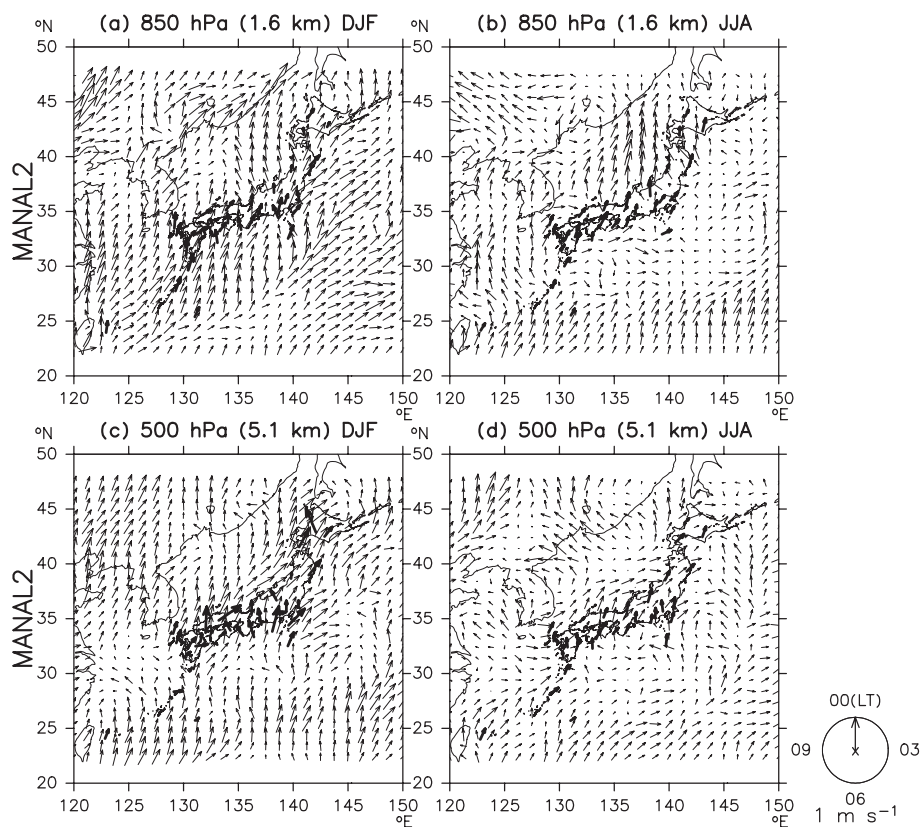


Fig. 7. As for Fig. 4, but for the semidiurnal component of  $v$  from WINDAS and MANAL2 data.

$\pi/6$  radians, and RMSEh is  $0.1\text{--}0.2\text{ m s}^{-1}$ . Thus, the semidiurnal wind component is also reproduced reasonably well in MANAL2.

Figure 7 shows the harmonic dial vectors of the semidiurnal wind component of  $v$  in DJF and JJA at 1.6 km (850 hPa) and 5.1 km (500 hPa) for WINDAS (MANAL2) data. The MANAL2 vectors show that the phase of the semidiurnal component of  $v$  is 0000–0200 LT for the whole analysis region, at both 850 and 500 hPa, and in both DJF and JJA. This phase is largely consistent with that in WINDAS and that of the theoretical semidiurnal migrating tide. The semidiurnal component of  $u$  in WINDAS is also reproduced reasonably well by MANAL2 (data not shown); the phase is 0300–0500 LT in MANAL, being preceded by that of  $v$  by a quadrature.

Figure 8 shows the month–pressure distributions of the MANAL2 semidiurnal amplitudes averaged for the 31 grid points closest to each WINDAS station. The amplitudes in both  $u$  and  $v$  attain maxima ( $0.4\text{--}0.5\text{ m s}^{-1}$ ) in winter–spring, largely consistent

with the results in WINDAS (Fig. 15 in SF10), both qualitatively and quantitatively, except that the amplitude in MANAL2 is largest at 900–850 hPa, particularly for  $v$ , being lower than the value derived from WINDAS data (4–5 km). In Fig. 7, the amplitude in DJF is larger than that in JJA for the entire analysis region, including Japan.

In summary, the spatial and seasonal characteristics of the WINDAS diurnal wind components reported by SF10 are reproduced reasonably well at both 1–3 km and 3–5 km, at least in MANAL1, JRA25, and ERA-Interim. The semidiurnal wind component is reproduced reasonably well in MANAL2.

#### 4. Results and discussion regarding the diurnal wind component

Here, we investigate the dynamical processes that control the diurnal wind component over Japan at 1–3 km (900–700 hPa) and 3–5 km (700–500 hPa), based mainly on MANAL1 and

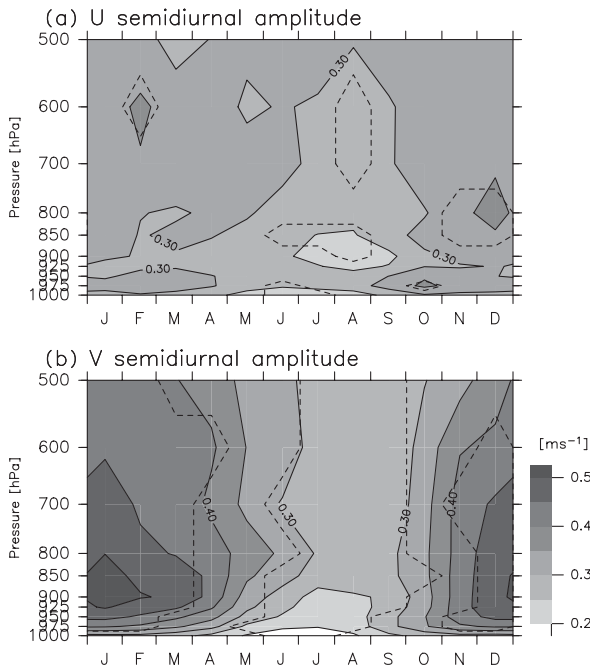


Fig. 8. As for Fig. 5, but for the semidiurnal amplitudes from MANAL2.

JRA25. We focus on the height region above  $\sim 1$  km, as below  $\sim 1$  km it is clear that local wind systems are the primary processes. In Section 4.1, based on MANAL1 data, we discuss the seasonal maxima in the diurnal wind component at 1–3 km found in spring and autumn, as reported by SF10. In Section 4.2, based on JRA25 data, we reveal the contribution of atmospheric tides to the diurnal wind component at 3–5 km height over the main Japanese islands, and throughout the entire lower

troposphere at stations on small southern islands. In Section 4.3, again based on JRA25 data, we confirm the suggestion made by SF10 that medium-scale eastward-traveling waves prevail at 3–5 km in winter–spring.

4.1 Return currents and diurnal eastward-moving eddies

WINDAS and MANAL1 data reveal that the diurnal amplitude at 850–700 hPa has maxima in spring and in autumn. Figure 9 shows the regions and time periods when the diurnal amplitude of  $v$  attains its maximum at 800 hPa ( $\sim 2$  km height), based on MANAL1 data. Along the north coast of Japan and over the Sea of Japan, the amplitudes tend to attain maxima in MAM, whereas along the south coast of Japan and in the Pacific south of Japan, the amplitudes tend to attain maxima in August–September–October (ASO). These features are also seen in the diurnal component of  $u$  (data not shown).

Figures 10–12 shows time series of the spatially high-pass filtered diurnal component of horizontal winds and geopotential height at 800 hPa in different seasons, as derived from MANAL1 data. Large-scale, low zonal-meridional-wavenumber components (i.e., tidal components) are defined using multiple regressions (i.e.,  $X = ax + by + c$ , where  $x$  and  $y$  are longitude and latitude, respectively) at each local time, and are subtracted from the original fields. We have confirmed that the regression components of winds are largely consistent with the tidal wind field in JRA25 (see Section 4.2) and that the distribution of spring and autumn maxima in Fig. 9 does not change considerably before or after this high-pass filtering process. In other

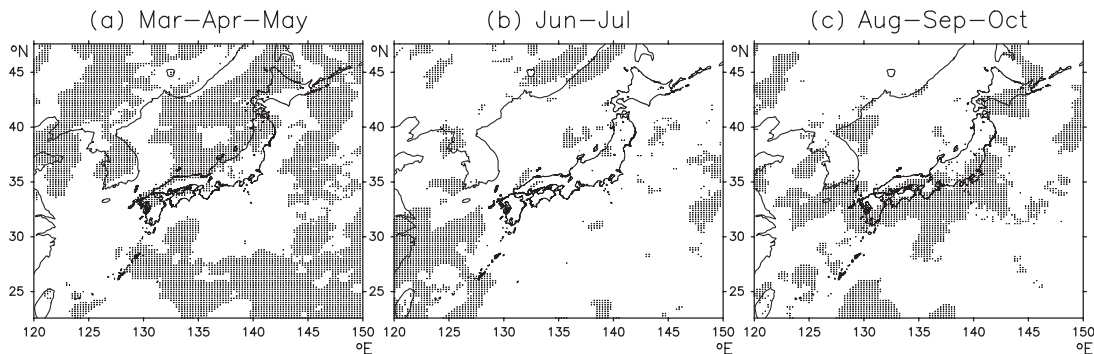


Fig. 9. Regions and time periods for which the diurnal amplitude of  $v$  attains a maximum at 800 hPa derived from MANAL1 data. Panel (a) shows such regions (dotted) in March–May, panel (b) in June–July, and panel (c) in August–October.

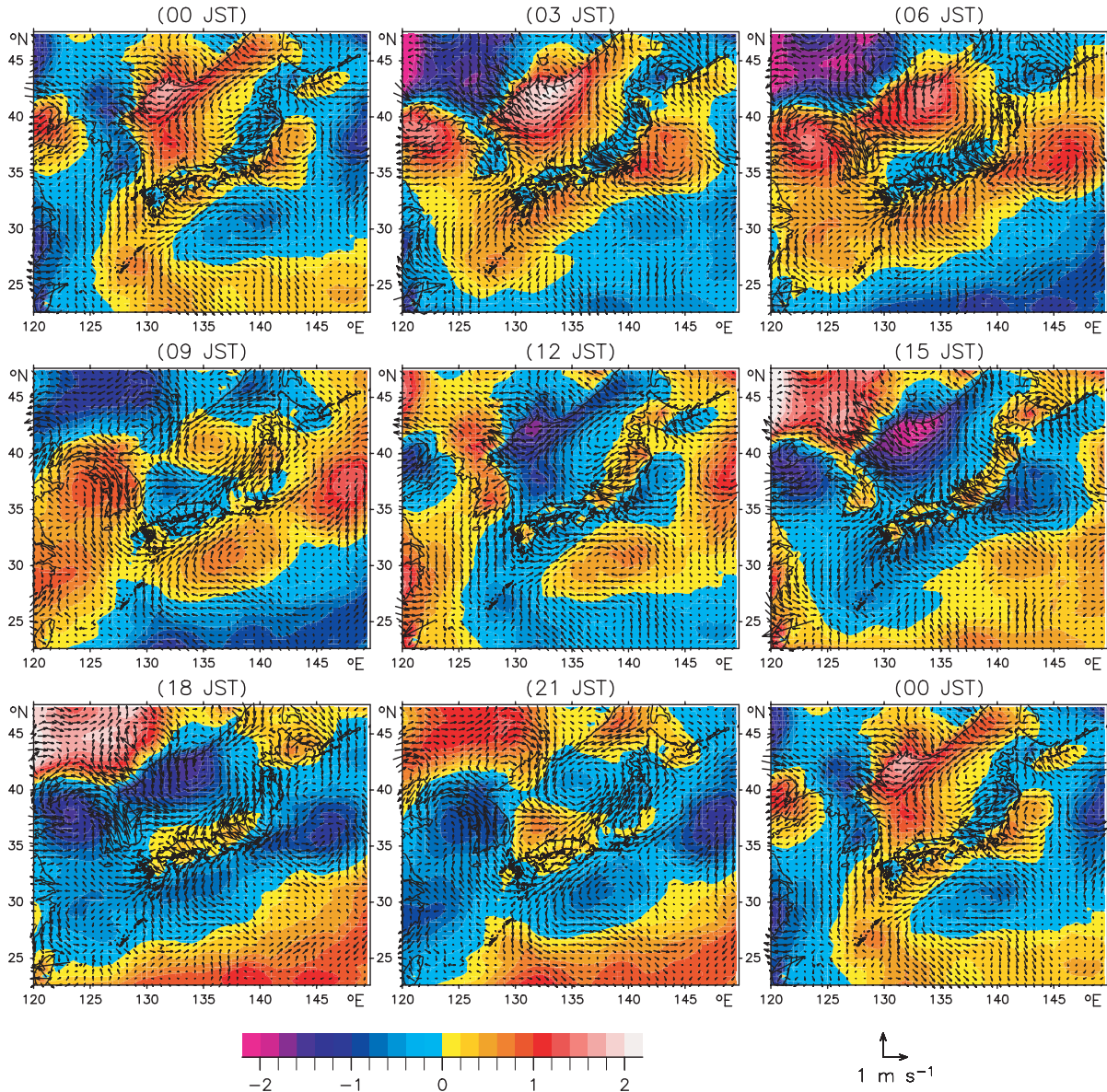


Fig. 10. Time series of the longitude–latitude distributions of the diurnal component of horizontal winds (vectors) and geopotential height (color scale) at 800 hPa in March–April–May (MAM), as derived from MANAL1 data at 0000 Japanese Standard Time (JST) to 2100 JST at 3-hour intervals. Three-hourly data were compiled from the harmonic diurnal component (see Section 2). A high-pass filter has been applied; see the text for details. A reference vector is shown at the bottom.

words, the spring and autumn maxima are primarily caused by smaller-scale disturbances, not by the diurnal tide. In Section 4.1.a, we describe the features of eastward-moving phenomena reported for the first time in this paper. Subsequently, the contribution of these phenomena to the diurnal wind component at 1–3 km is discussed in Section 4.1.b.

#### a. Diurnal eastward-moving eddies

Figures 10–12 show that eddies with a horizontal scale of  $\sim 700$  km move eastward over the Japan region throughout the year. In MAM (Fig. 10), a region with large geopotential height (hereafter,  $Z$ ) first appears at 0000 Japanese Standard Time (JST) in the northwesternmost part of the Sea of

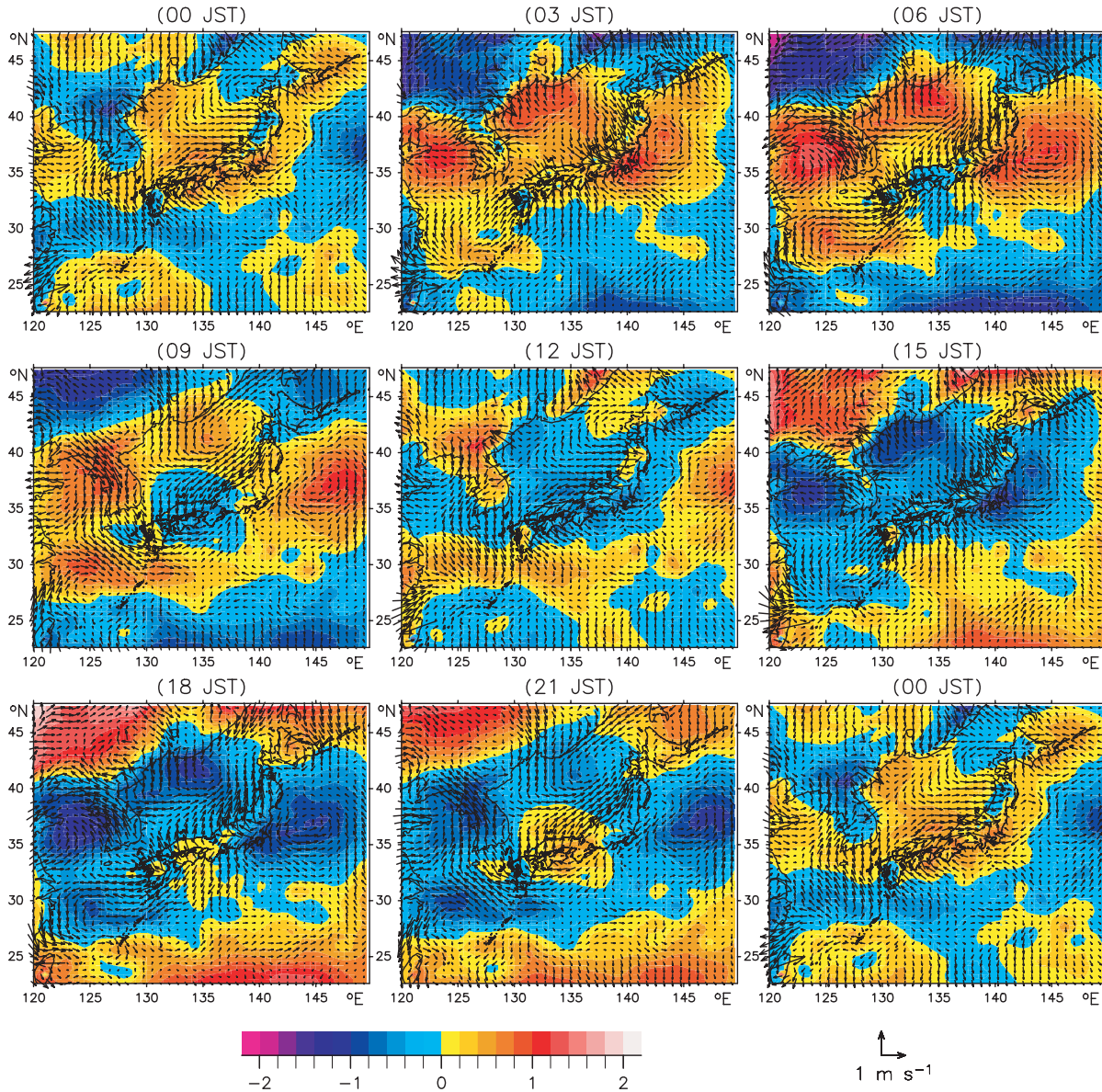


Fig. 11. As for Fig. 10, but in May–June–July (MJJ).

Japan, at around (42°N, 132°E). The region of high  $Z$  propagates eastward, accompanied by anticyclonic winds. The center of this anticyclonic eddy is at (43°N, 133°E) at 0300 JST, (41°N, 134°E) at 0600 JST, (41°N, 135°E) at 0900 JST, and reaches (41°N, 138°E) at 1200 JST. The phase velocity is estimated to be  $\sim 15 \text{ m s}^{-1}$  based on a Hovmoller diagram for  $v$  (data not shown). This speed is approximately consistent with that estimated from the phase propagation at 1.9 km in February in WINDAS ( $\sim 20 \text{ m s}^{-1}$ ), as reported by SF10.

Therefore, we suggest that the eastward phase propagation at 1.9 km in winter–spring, as reported by SF10, is due to this eddy. The diameter of the eddy is estimated to be  $\sim 700 \text{ km}$ . Hereafter, this type of eddy is referred to as a “Diurnal Eastward-moving Eddy (DEE),” and the DEE over the Sea of Japan, as described above, is referred to as “DEE-a”. DEE-a is also found in other seasons. In May–June–July (MJJ) (Fig. 11), the positive  $Z$  region for DEE-a travels eastward at the same latitude region and at the same phase

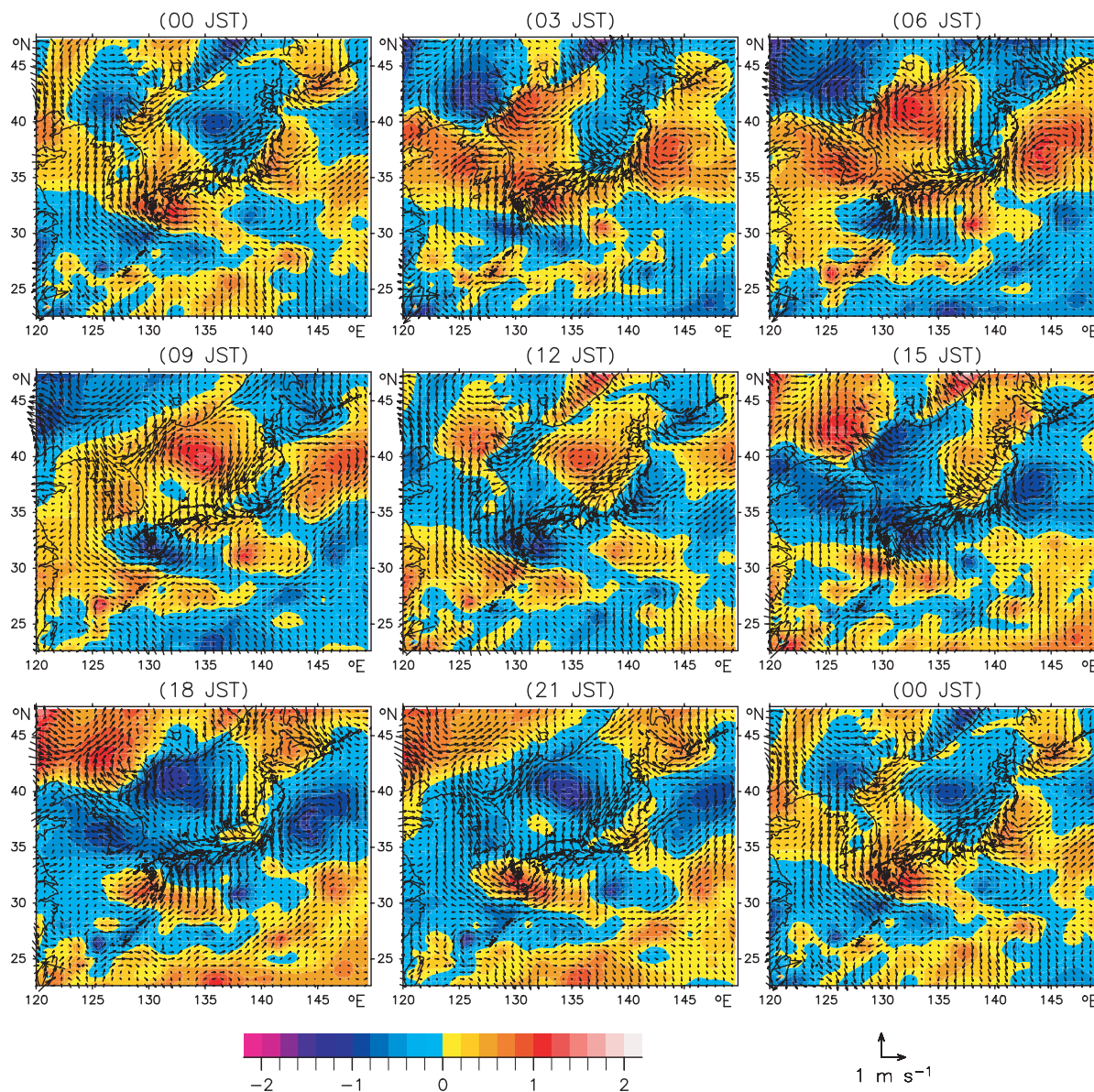


Fig. 12. As for Fig. 10, but in August–September–October (ASO).

speed as in MAM. However, the amplitude of  $Z$  for DEE-a in MJJ is only half that in MAM (e.g., at 0300 JST). In ASO (Fig. 12), the location of DEE-a at a given time is different from that in MAM and MJJ, although the phase speed is similar. For example, at 0900 JST, DEE-a is found at  $134^{\circ}\text{E}$  in ASO, but at  $136^{\circ}\text{E}$  in MAM and MJJ. In addition, in ASO, DEE-a tends to sustain its original strength during eastward propagation. For example, the positive  $Z$  region of DEE-a at 1200 JST has a value of  $\sim 1$  m in ASO, whereas DEE-a is not evident at 1200 JST in MAM and MJJ.

Figure 13 (left panels) shows a time series of the longitude–pressure distributions of the diurnal component of  $v$  and  $Z$  at  $41^{\circ}\text{N}$  in ASO, where and when DEE-a develops (Fig. 12), from 0000 JST to 0900 JST at 3-hour intervals. At 0000 JST, a positive  $Z$  region appears at 850–700 hPa, along the eastern slope of high mountains upon the east coast of the Eurasian Continent ( $\sim 130^{\circ}\text{E}$ ). At 0300–0600 JST, the positive  $Z$  develops up to 500 hPa and extends eastward. The diurnal component of  $v$  is also strong up to 800–500 hPa, being in geostrophic balance with the westward pressure gradient at

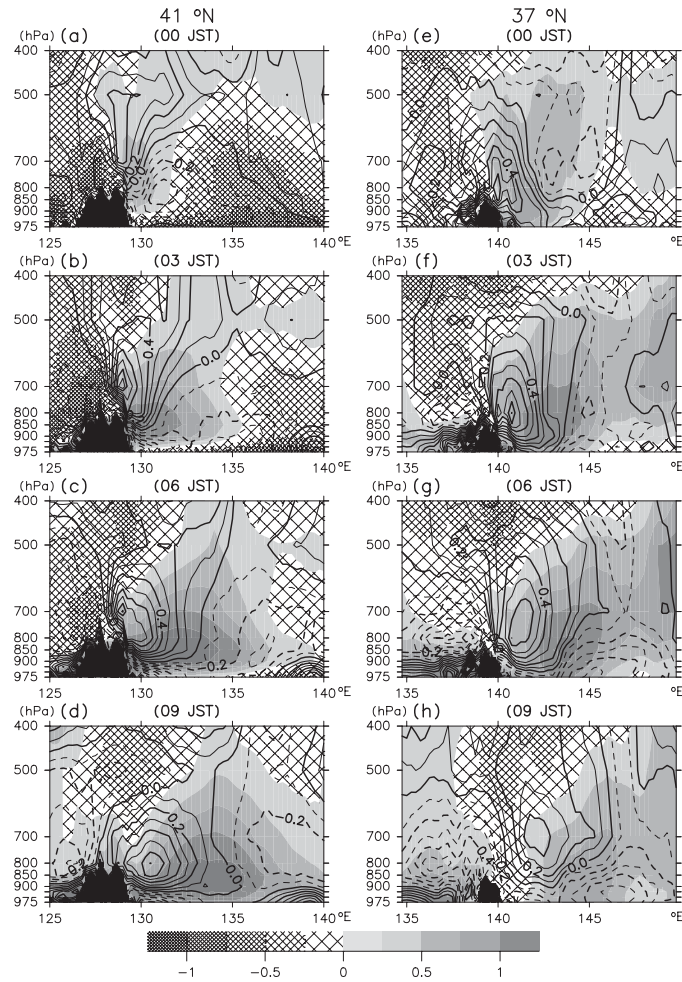


Fig. 13. Longitude–pressure distributions of the diurnal component of  $v$  (contours) and  $Z$  (gray scale), as derived from MANAL1 data at (a) 00 JST, (b) 03 JST, (c) 06 JST, and (d) 09 JST along  $41^\circ\text{N}$  between  $125^\circ\text{E}$  and  $140^\circ\text{E}$ , and at (e) 00 JST, (f) 03 JST, (g) 06 JST, and (h) 09 JST along  $37^\circ\text{N}$  between  $135^\circ\text{E}$  and  $150^\circ\text{E}$ , in August–September–October (ASO). Black shading indicates the topography. Three-hourly data were compiled from the harmonic diurnal component (see Section 2).

$\sim 130^\circ\text{E}$ . At 0900 JST, the positive  $Z$  and associated  $v$  propagate further eastward to  $\sim 133^\circ\text{E}$ , with their center being near the surface (900–800 hPa). DEE-a has a barotropic structure up to 700–500 hPa.

Two other DEEs were observed along the east and south coasts of Japan. Figure 10 shows that one of the DEEs (DEE-b) propagates eastward from the east coast of Japan ( $37^\circ\text{N}$ ,  $143^\circ\text{E}$ ) at 0000 JST, through ( $37^\circ\text{N}$ ,  $144^\circ\text{E}$ ) at 0300 JST and ( $37^\circ\text{N}$ ,  $146^\circ\text{E}$ ) at 0600 JST, to ( $38^\circ\text{N}$ ,  $148^\circ\text{E}$ ) at 0900 JST. The other DEE (DEE-c) propagates from the south coast of Japan at ( $32^\circ\text{N}$ ,  $133^\circ\text{E}$ ) at 0300 JST, through ( $31^\circ\text{N}$ ,  $135^\circ\text{E}$ ) at 0600 JST and ( $30^\circ\text{N}$ ,  $137^\circ\text{E}$ ) at 0900 JST, to ( $30^\circ\text{N}$ ,  $139^\circ\text{E}$ )

at 1200 JST. Both eddies have a diameter of  $\sim 700$  km. The zonal phase speed is estimated to be  $10$ – $15$   $\text{m s}^{-1}$  based on a Hovmöller diagram. DEE-b is also observed in MJJ and ASO, affecting the diurnal wind component over Japan, as shown in the following section. DEE-c is only observed in MAM.

Figure 13 (right panels) also shows a time series of the longitude–pressure distributions of the diurnal component of  $v$  and  $Z$  at  $37^\circ\text{N}$  in ASO, where and when DEE-b develops (Fig. 12). The characteristics of DEE-b are similar to those of DEE-a. At 0000 JST, a positive  $Z$  region appears near the east coast of Japan at  $\sim 140^\circ\text{E}$  in the height region from 975 hPa to 700–500 hPa. At 0300 JST, the region

of positive  $Z$  has developed and moved eastward to  $\sim 143^\circ\text{N}$ . The diurnal component of  $v$  is strong up to 700–500 hPa, being in geostrophic balance with the zonal pressure gradient ( $\sim 140^\circ\text{E}$ ) associated with DEE-b. At 0600–0900 JST, the positive  $Z$  and associated  $v$  propagate further eastward, with their center near the surface (900–700 hPa). DEE-b has a barotropic structure up to 700–500 hPa, as with DEE-a.

Thus, it is confirmed that at least three DEEs, with diameters of  $\sim 700$  km, prevail around Japan throughout the year. The DEEs are generated on the eastern side of high mountainous regions (either on the eastern edge of the Eurasian Continent or in Japan) and move eastward over the ocean with a zonal phase speed of  $10\text{--}15\text{ m s}^{-1}$ . The pressure and velocity fields largely satisfy the geostrophic relationship. In addition, the DEEs are confined to below  $\sim 700$  hPa ( $\sim 3$  km), showing a barotropic structure. Note that the strength and temporal/spatial configuration of the DEEs show a strong seasonal variation, which is a key feature in terms of understanding seasonal variations in the diurnal wind component over Japan, as will be shown in the following section.

The DEEs are different from the medium-scale waves that develop in the upper troposphere (Sato et al. 1993; see also Section 4.3): the zonal wavelength ( $\sim 1500$  km: double the horizontal scale of an eddy) and the zonal wave velocity ( $10\text{--}15\text{ m s}^{-1}$ ) of DEEs are smaller than those of medium-scale waves (2000–3000 km and  $25\text{ m s}^{-1}$ , respectively). In addition, the DEEs are confined to the lower troposphere.

#### *b. Contribution of DEEs to the diurnal wind component over Japan*

Here, we discuss the contribution of DEEs to seasonality in the diurnal amplitude over the main Japanese islands. During the nighttime (0000–0600 JST) at 800 hPa in MAM (Fig. 10), geopotential height,  $Z$ , is negative ( $\sim -0.5$  m) over the main Japanese islands, while  $Z$  is positive over the adjacent sea. In contrast,  $Z$  at 975 hPa has large positive values ( $\sim 2$  m) over the main Japanese islands during the nighttime (data not shown). Thus, during the nighttime, the pressure gradient forces are offshore at 975 hPa and onshore at 800 hPa. These forces at 975 and 800 hPa control the local surface winds (i.e., land–sea breezes) and their return currents, respectively. In fact, at 800 hPa (Fig. 10), the winds are basically onshore at 0000–0600 JST

and offshore at 1200–2100 JST over the main Japanese islands. In addition, we find a large pressure gradient over the Sea of Japan at 0000–0600 JST, due to DEE-a. The anticyclonic winds oriented normal to the pressure gradient (i.e., geostrophic winds) are southwestward at 0300–0600 JST, being onshore along the north coast. As a result of this in-phase relationship, the winds associated with DEE-a act to strengthen the return currents along the north coast, and the diurnal component has large amplitudes. The strong winds along the north coast extend to the south coast, being in phase with the surface wind system. This result explains the finding by SF10 that the surface wind system extends up to 1.5 km in MAM.

In MJJ (Fig. 11), the low pressure system at 800 hPa over the main Japanese islands during the nighttime is weaker than that in MAM. Tijn et al. (1999) showed that the strength of the return currents relative to that of the surface winds is dependent on the strength of the inversion above the boundary layer. Thus, the weaker pressure gradient between land and sea at 800 hPa in MJJ may be due to seasonal variations in the vertical profile of temperature; i.e., weaker stability in summer. In addition to the weakness of the return currents, the winds at 0300–0600 JST associated with DEE-a are slightly weaker than those in MAM; consequently, the onshore/offshore winds along the north coast in MJJ are not as strong as those in MAM. In contrast, the return currents along the south coast in MJJ are stronger than those in MAM because of the minor influence of winds from DEE-a. In MJJ, the onshore (offshore) return currents from the north and south coasts converge (diverge) over the main Japanese islands during the nighttime (daytime). In addition, these return currents do not appear to feel the “local” coast but seem to be controlled mainly by larger-scale ( $\sim 100$  km) pressure gradient forces (i.e., the contrast between the main Japanese islands and adjacent sea), as suggested in SF10.

Finally, in ASO (Fig. 12), the nighttime pressure gradient between the main Japanese islands and the adjacent sea is not as clearly pronounced as that in MAM, as is the case in JJA. Note that we see a negative  $Z$  region of DEE-a centered at ( $40^\circ\text{N}$ ,  $136^\circ\text{E}$ ) and at ( $40^\circ\text{N}$ ,  $138^\circ\text{E}$ ), at 0000 JST and 0300 JST, respectively. At the same time, a positive  $Z$  region of DEE-b starts to develop at ( $37^\circ\text{N}$ ,  $143^\circ\text{E}$ ) at 0300 JST. Thus, the pressure gradient force strengthens in a northwest–southeast orienta-

tion at 135–140°E over Japan, generating strong northward geostrophic winds, particularly over southeastern Japan during the nighttime (0000–0300 JST). These winds are basically in phase with the return currents along the south coast, resulting in large amplitudes in this region.

In DJF (data not shown), the return currents are observed even though their amplitudes are small. The main Japanese islands are influenced mainly by the winds associated with DEE-a, as inferred by SF10.

Finally, we briefly describe the results obtained from global reanalysis data. DEE-a is observed at 850 hPa (800 hPa) in JRA25 (ERA-Interim) throughout the year. The characteristics in JRA25 and ERA-Interim (e.g., location, horizontal scale, and phase speed) are basically the same as those in MANAL1, except that the strength in  $Z$  of DEE-a in ERA-Interim is half that in MANAL1 and JRA25. DEE-a generates large diurnal amplitudes along the north coast during MAM in JRA25 and ERA-Interim. In JRA25, DEE-b propagates in the same way as that in MANAL1 in summer–autumn, although the amplitude of  $Z$  is only half that in MANAL1. In JRA25, DEE-a and DEE-b generate strong geostrophic winds in ASO, resulting in large diurnal amplitudes along the south coast. DEE-b is barely observed in ERA-Interim, and DEE-c is not observed in JRA25 or ERA-Interim. Finally, no DEEs (i.e., DEE-a, DEE-b, or DEE-c) are observed in NCEP1 or NCEP2.

In summary, at 800 hPa ( $\sim 2$  km), the return currents of the local wind systems, which are onshore (offshore) during the nighttime (daytime), prevail throughout the year. In addition, we discovered that around Japan, DEEs with a horizontal scale of  $\sim 700$  km develop at regions with high mountains and thereafter travel eastward with a zonal phase speed of  $\sim 10$ – $15$  m s $^{-1}$ . The diurnal wind component at 800 hPa over the main Japanese islands is determined by the superposition of the return currents and the winds associated with DEEs. In spring, the DEE that develops and travels over the Sea of Japan acts to strengthen the return currents along the north coast. In autumn, the pressure gradient between two DEEs acts to strengthen the return currents along the south coast.

#### 4.2 Diurnal tide

Here, we examine the contribution to the diurnal wind component of the atmospheric diurnal tide,

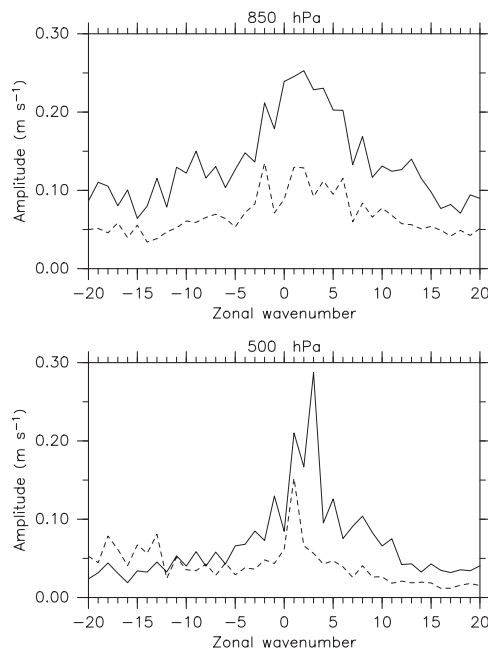


Fig. 14. Diurnal amplitudes of  $v$  for each zonal wavenumber averaged for 25–45°N at (top) 850 hPa and at (bottom) 500 hPa derived from JRA25 data. Solid lines are for June–July–August (JJA), and dashed lines are for December–January–February (DJF). The positive and negative wavenumbers correspond to components propagating westward and eastward, respectively.

based on JRA25 data. The three other reanalysis data sets (ERA-Interim, NCEP1, and NCEP2) yield similar results to those in JRA25 regarding the amplitude of each zonal wavenumber component (Fig. 14) and the horizontal distribution of tidal amplitudes and phases (Fig. 15) for both  $u$  and  $v$ .

Figure 14 shows the diurnal amplitude  $\sqrt{a_s^2 + b_s^2}$  of  $v$  for each zonal wavenumber  $s$  in Eq. (1) averaged for the latitude region from 25°N to 45°N at 850 and 500 hPa in DJF and JJA, based on JRA25 data. Large amplitudes are confined to  $-6 \leq s \leq 6$  at 500 hPa. The amplitudes at 850 hPa are more broadly distributed than those at 500 hPa. Based on these findings, we define the diurnal tide as the diurnal wind component reconstructed from the components of  $(-10 \leq s \leq 10)$  in Eq. (1). The ratio of variance for  $-10 \leq s \leq 10$  to the total variance is 0.56 (0.61) in DJF (JJA) at 850 hPa, and is 0.53 (0.83) in DJF (JJA) at 500 hPa. The relatively

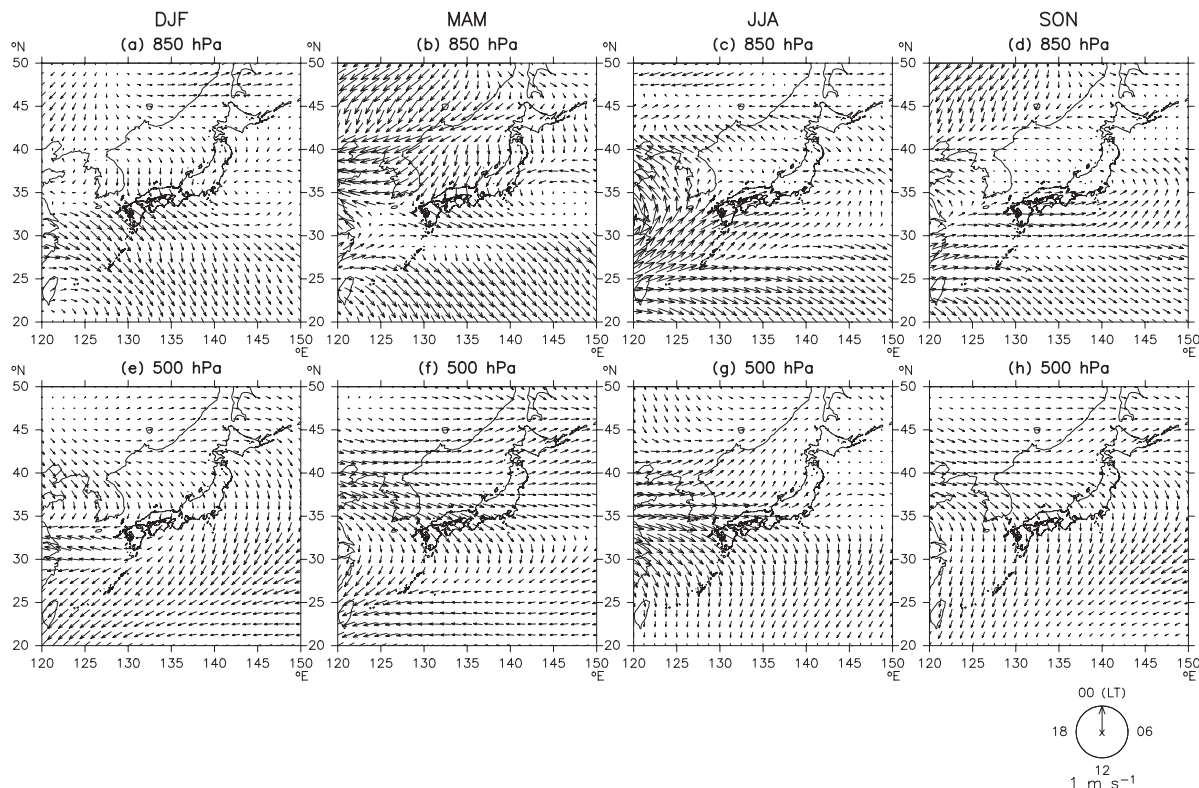


Fig. 15. Harmonic dial vectors of the diurnal tidal component of  $v$  with zonal wavenumbers of  $-10 \leq s \leq 10$ , as derived from JRA25 data for (a) December–January–February (DJF), (b) March–April–May (MAM), (c) June–July–August (JJA), and (d) September–October–November (SON) at 850 hPa, and for (e) DJF, (f) MAM, (g) JJA, and (h) SON at 500 hPa. Reference harmonic dial vectors are shown at bottom right. See the text for details.

low rate at 500 hPa in DJF is due in part to the large amplitudes for  $-20 \leq s \leq -10$ , which result from the medium-scale waves discussed in Section 4.3. Note that in the tidal model GSWM02, the tide is defined as the components of  $-6 \leq s \leq 6$ . We confirmed that a change in the definition of tide to ( $-6 \leq s \leq 6$ ) has no qualitative effect on the below results for the entire latitude region at 500 hPa and for the latitude region equatorward of  $\sim 30^\circ\text{N}$  at 850 hPa. Figure 14 shows that among the tidal components, the migrating component ( $s = 1$ ) is large but not the largest, and the other nonmigrating components make a relatively large contribution to the diurnal tide, particularly at 850 hPa.

Figure 15 shows harmonic dial vectors for the diurnal tidal component of  $v$  at 850 and 500 hPa, based on JRA25 data. At 850 hPa and equatorward of  $\sim 33^\circ\text{N}$ , the tidal phase and amplitude are 0600–0900 LT and  $\sim 0.5 \text{ m s}^{-1}$ , respectively, throughout the year. Note that for the region of

( $25\text{--}30^\circ\text{N}$ ,  $120\text{--}130^\circ\text{E}$ ), the tidal amplitude reaches  $\sim 1.0 \text{ m s}^{-1}$  in JJA. At 850 hPa and poleward of  $\sim 33^\circ\text{N}$ , the tidal amplitude is small ( $< 0.2 \text{ m s}^{-1}$ ) except in MAM, when the phases and amplitudes over the Sea of Japan are 1200–1500 LT and  $\sim 0.5 \text{ m s}^{-1}$ , respectively.

At 500 hPa, the tidal phase is markedly different ( $\sim 6 \text{ hr}$ ) between the regions poleward and equatorward of  $\sim 35^\circ\text{N}$ . The phase is 0900–1200 LT (1400–1800 LT) poleward (equatorward) of  $35^\circ\text{N}$  in DJF, and is 0300–0600 LT (0900–1200 LT) in JJA, showing regional and seasonal variations. The tidal amplitude is  $\sim 0.5 \text{ m s}^{-1}$  throughout the year, being relatively large in areas equatorward of  $\sim 35^\circ\text{N}$ .

An analysis of tidal component of  $u$  yields similar results to those above, except that the phase of  $u$  is  $\sim 6 \text{ hr}$  later than that of  $v$  and the wind vectors rotate clockwise. This phase relationship is largely consistent with tidal theory.

Next, we estimate the contribution of the diurnal tide to the diurnal wind component over Japan, by comparing the results in Fig. 4 (for JRA25) with those in Fig. 15. At 850 hPa, the tidal amplitudes and phases (Figs. 15a, c) match those of the original JRA25 vectors (Figs. 4e, f) for regions equatorward of 30°N, including stations on small southern islands. Therefore, we conclude that the diurnal wind component at these islands is controlled primarily by the diurnal tide throughout the year, even near the surface. In JJA, at 850 hPa, stations on Kyushu (30–35°N, 128–132°E) are also controlled mainly by the diurnal tide, as inferred in Section 3.2.b. Furthermore, along the north (south) coast of the main Japanese islands in MAM (JJA), the tidal component with an amplitude of  $\sim 0.2 \text{ m s}^{-1}$  is approximately in phase with the return currents (Figs. 15b, c), meaning that the diurnal tide acts to strengthen the diurnal wind component to some extent in these regions and seasons.

At 500 hPa in JJA, the tidal amplitudes and phases (Fig. 15g) basically match those of the diurnal amplitudes and phases (Fig. 4h) over both the main Japanese islands and small southern islands; this finding also applies in SON (data not shown). Therefore, we conclude that the large-scale diurnal wind system reported by SF10 above 3–4 km in JJA–SON is due primarily to the diurnal tide over all of Japan. An analysis of  $u$  yields similar results (data not shown). In DJF, in contrast, the tidal vectors of  $v$  (Fig. 15e) do not match the original JRA25 vectors (Fig. 4g), except for small southern islands at  $\sim 25^\circ\text{N}$ . The tidal vectors of  $u$  in DJF basically match the original vectors, except for the latitude region of  $\sim 40^\circ\text{N}$ , where eastward phase propagation is observed (data not shown). In other words, the difference in the phase of  $u$  between stations located along the north and south coasts in DJF, as reported in SF10, is explained by the tidal components.

Here, we discuss the excitation mechanism of the diurnal tide. For regions equatorward of 30°N, including stations on small southern islands, an analysis of vertical profiles of the JRA25 tidal phase shows that the phases have basically positive slopes below 5–10 km (10–20 km) in DJF (JJA) and negative slopes above these levels (data not shown). These findings indicate that the excitation sources exist in the middle–upper troposphere, from which energy propagates both upward and downward. The vertical wavelengths below 5 km are small

( $\sim 10 \text{ km}$ ) in DJF and large ( $\sim 20 \text{ km}$ ) in JJA (data not shown), being consistent with the WINDAS results at small southern island stations (SF10). These phase structures in JRA25, including their seasonal variations, are basically consistent with those of the diurnal tide excited by radiative heating of water vapor (see Fig. 20 in Lieberman and Leovy 1995). The GSWM02 results, which consider radiative heating of ozone, and water vapor and latent heat release as excitation sources, show similar phase structures, although the absolute phase values are inconsistent with our results, as shown in the following paragraph. Thus, the diurnal tide for this latitude region would be primarily excited by radiative heating of tropospheric water vapor and/or latent heat release. In addition, the small longitudinal variability of tidal phases in these regions (Fig. 15) indicates the primary importance of the migrating component. It is inferred that the long wavelengths in JJA show the dominance of the principal Hough mode of the migrating component and that the small wavelengths in DJF show the non-negligible influence of high-order Hough modes of the migrating component. For regions poleward of  $\sim 30^\circ\text{N}$ , including the main Japanese islands, the large horizontal variability of tidal components at 850 hPa (Figs. 15a–d) indicates the dominance of nonmigrating components throughout the year, which would be excited by sensible heating from the planetary boundary layer. An analysis of profiles of JRA25 tidal phase reveals that above 700 hPa ( $\sim 3 \text{ km}$ ), the phase structures are similar to those for regions equatorward of 30°N. Thus, it is inferred that the diurnal tide at 3–5 km for these regions is that excited by radiative heating by tropospheric water vapor and/or latent heat release, as is the case for regions equatorward of  $\sim 30^\circ\text{N}$ .

SF10 showed that the tidal phase at 4 km height in the tidal model GSWM02 is 1800 LT (1200 LT) for  $u$  ( $v$ ) at 20–50°N throughout the year. These phases are largely consistent with the JRA25 tidal phases equatorward of 30°N at 500 hPa, particularly in JJA (Fig. 15). However, the seasonal variations in tidal phase shown in JRA25 are not reproduced in GSWM02. Furthermore, the tidal phases over the main Japanese islands (e.g.,  $\sim 0600 \text{ LT}$  in JJA) are not reproduced in GSWM02. This finding raises the possibility that the inconsistency in the diurnal wind component between WINDAS and GSWM02 at 500 hPa, as reported in SF10, occurs because of the poor reproducibility of the diurnal

tide in GSWM02, at least over the main Japanese islands. The poor reproducibility may result in part from the lack of boundary layer heating in GSWM02, which is the main source of diurnal tides near the surface (Tsuda and Kato 1989; Lieberman and Leovy 1995), in part from the contrasting definitions of tides used in the present study and in GSWM02 (M. Hagan 2009, personal communication), and in part from the inaccuracy of the excitation sources (water vapor and/or latent heat release) in GSWM02.

In summary, we define the diurnal tide as the diurnal component with zonal wavenumbers of  $-10 \leq s \leq 10$ . For the region equatorward of  $\sim 30^\circ\text{N}$ , including small southern islands, the diurnal wind component is controlled primarily by the diurnal tide, over the entire lower troposphere throughout the year. Over the main Japanese islands, the diurnal tide is predominant at 3–5 km in JJA–SON, as well as in some areas below 3 km (e.g., over Kyushu in JJA). The diurnal component at 3–5 km in DJF, in contrast, is not explained by the diurnal tide over the main Japanese islands, particularly for  $v$ .

#### 4.3 Medium-scale eastward-traveling waves

In the previous section, we found that the diurnal wind component (particularly  $v$ ) at 500 hPa in DJF is not explained by the diurnal tide. At this height region, WINDAS measurements (SF10) suggest that medium-scale eastward-traveling waves control the diurnal wind component over Japan in DJF–MAM. The zonal phase speed and amplitude at 5.1 km are estimated to be  $\sim 25 \text{ m s}^{-1}$  and  $\sim 0.8 \text{ m s}^{-1}$ , respectively. Here, we confirm the contribution of medium-scale waves to the diurnal wind component based on an analysis of JRA25 data. Analyses of other global reanalysis data sets (ERA-Interim, NCEP1, and NCEP2) yield similar results for these waves.

Figure 16 shows a time series of longitude–height distributions of the diurnal component of  $v$ , averaged at  $35\text{--}40^\circ\text{N}$  from 0600 JST to 1500 JST in February, based on JRA25. We observe a clear wave train with a zonal wavelength of  $\sim 2300 \text{ km}$ , ranging from 700 to 200 hPa with a maximum in the upper troposphere ( $\sim 300 \text{ hPa}$ ). The vertical structure is barotropic in this height region. These waves travel eastward at a zonal phase speed of  $\sim 25 \text{ m s}^{-1}$  (e.g., at 300 hPa, a maximum at  $128^\circ\text{E}$  at 0600 JST moves eastward to  $137^\circ\text{E}$  at 1500 JST). At 500 hPa, the amplitude is  $\sim 0.7 \text{ m s}^{-1}$  over

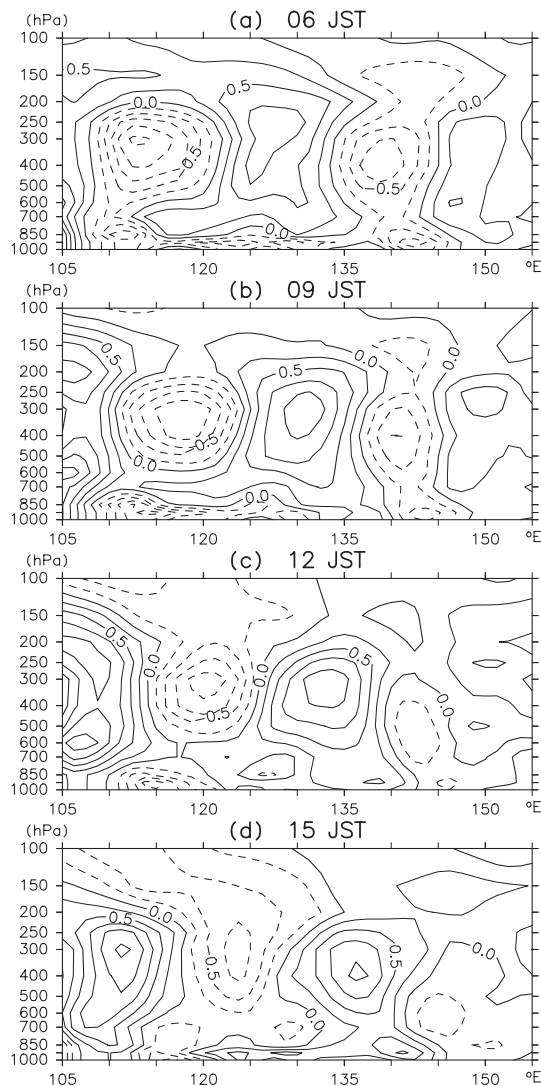


Fig. 16. Longitude–height distributions of the diurnal component of  $v$  averaged for  $35\text{--}40^\circ\text{N}$  in February, as derived from JRA25 data at (a) 0600 JST, (b) 0900 JST, (c) 1200 JST, and (d) 1500 JST. The contour interval is  $0.25 \text{ m s}^{-1}$ . Three-hourly data were compiled from the harmonic diurnal component (see Section 2).

Japan (e.g., at  $135^\circ\text{N}$  in Fig. 16c). These characteristics are largely consistent with the WINDAS measurements presented by SF10, and are consistent with the medium-scale waves in the upper troposphere reported by Sato et al. (1993), although the maximum amplitude at the tropopause in the present study ( $\sim 1 \text{ m s}^{-1}$ ) is somewhat smaller than

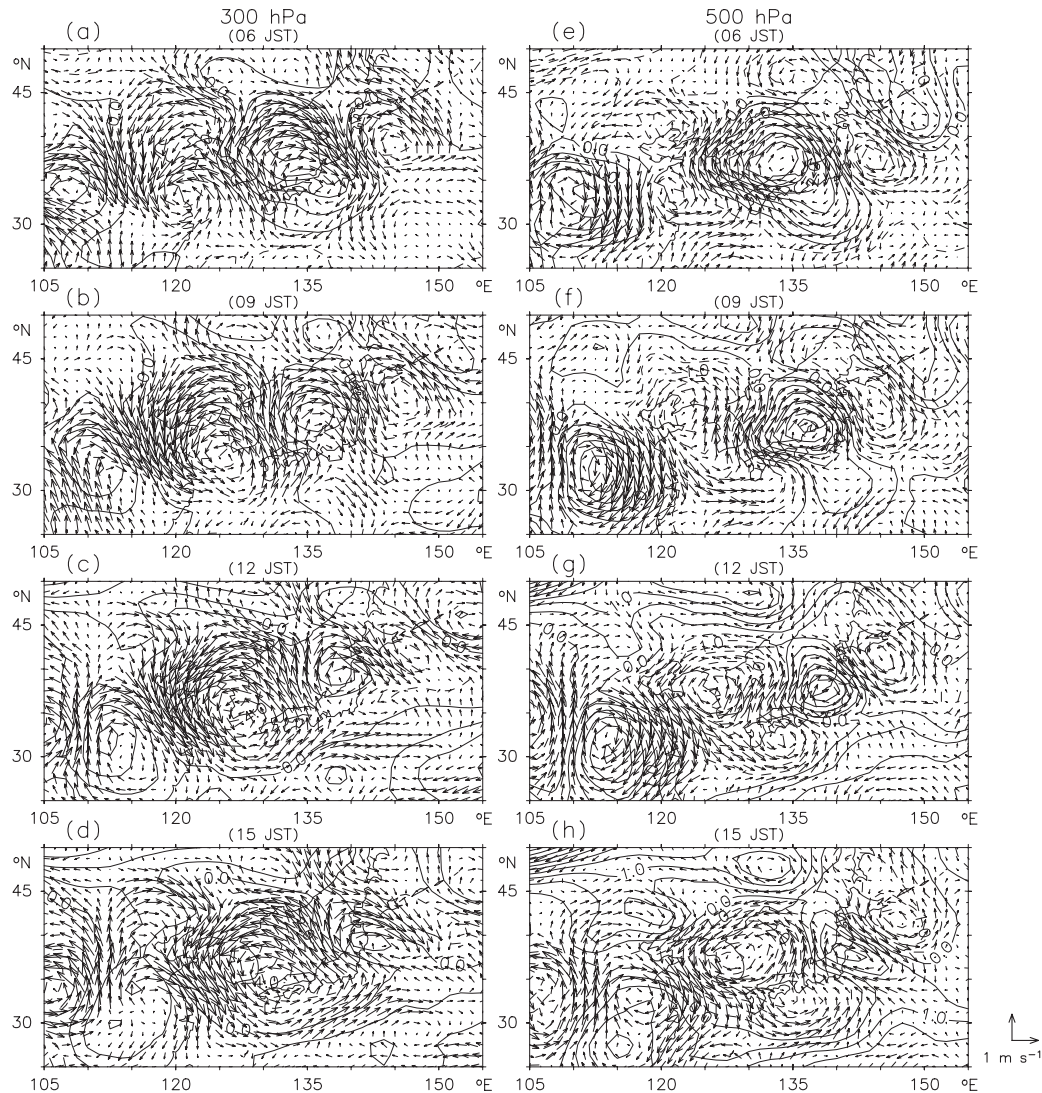


Fig. 17. Longitude–latitude distributions of the diurnal component of horizontal winds (vectors) and geopotential height (contours) in February, as derived from JRA25 at (a) 0600 JST, (b) 0900 JST, (c) 1200 JST, and (d) 1500 JST at 300 hPa, and at (e) 0600 JST, (f) 0900 JST, (g) 1200 JST, and (h) 1500 JST at 500 hPa. Three-hourly data were compiled from the harmonic diurnal component. The contour interval for geopotential height is 1 m for (a–d) and 0.5 m for (e–h). A high-pass filter was applied; see the text for details. A reference vector is shown at bottom right.

that reported by Sato et al. (1993) ( $\sim 5 \text{ m s}^{-1}$ ). Thus, we conclude that the diurnal component of  $v$  at 3–5 km in DJF–MAM is controlled mainly by medium-scale waves. Note that the winds associated with DEE-a are also observed in Fig. 16 around 850–700 hPa: a maximum at  $\sim 133^\circ\text{E}$  at 0600 JST travels to  $\sim 135^\circ\text{E}$  at 0900 JST and to  $\sim 136^\circ\text{E}$  at 1200 JST, reaching  $\sim 140^\circ\text{E}$  at 1500 JST.

Next, we examine the horizontal structures of these waves in order to determine the horizontal

distribution of their influence. Figure 17 shows a time series of the longitude–latitude distributions of the diurnal component of horizontal winds and geopotential height at 300 and 500 hPa in February, based on JRA25. As in Figs. 10–12, the multiple regressions have been removed. At 300 hPa, waves with a horizontal scale of  $\sim 2000 \text{ km}$  travel eastward over Japan. For example, cyclonic winds centered at  $(35^\circ\text{N}, 122^\circ\text{E})$  at 0600 JST travel to  $(35^\circ\text{N}, 132^\circ\text{E})$  at 1500 JST. These waves are

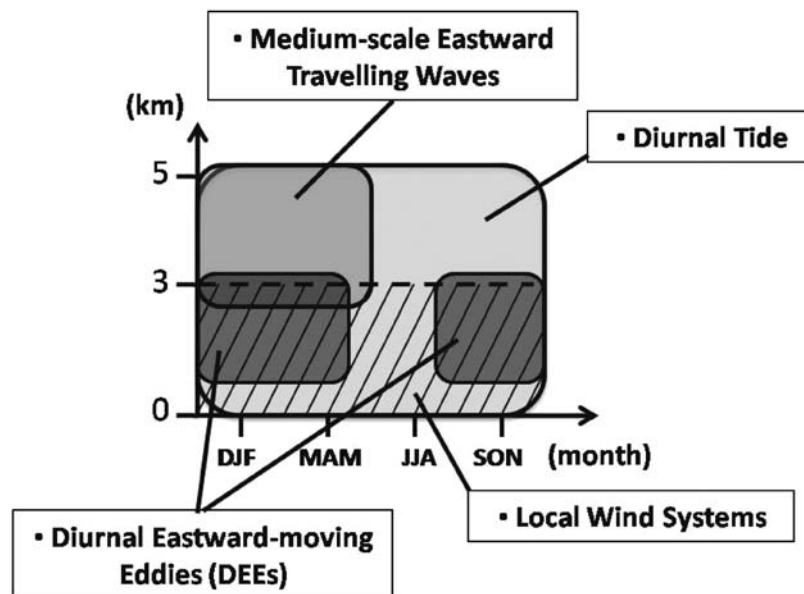


Fig. 18. Month–height distributions of the primary dynamical processes that control the diurnal wind component over the main Japanese islands. See the text for details.

confined to the latitude region of 30–45°N. The winds and geopotential height generally satisfy the geostrophic balance, consistent with the finding reported by Sato et al. (1993).

The wavy structure is also seen at 500 hPa, at which height the locations of the northward winds are the same as those at 300 hPa. Note that the zonal winds associated with these waves are strong in the latitude regions of 38–43°N and 25–30°N, while the meridional winds are strong at 30–40°N (e.g., Fig. 17e). This latitudinal dependency explains why, based on WINDAS measurements, SF10 observed eastward-propagating signals in  $v$  at  $\sim 30$ –40°N, while those in  $u$  are seen only around 40°N. Note that for most of the main Japanese islands, the diurnal component in  $u$  is explained largely in terms of the diurnal tide, as shown in Section 4.2.

In summary, the diurnal wind component over Japan at 3–5 km in DJF–MAM is controlled mainly by medium-scale waves with amplitude maxima in the upper troposphere. At 500 hPa, medium-scale waves have large amplitudes at  $-20 \leq s \leq -10$  (eastward-traveling components with a zonal wavelength of 1500–3000 km) in DJF (Fig. 14).

## 5. Concluding remarks

Following on from SF10, we studied diurnal variations in lower-tropospheric wind over Japan,

using JMA mesoscale analysis (MANAL) data and four global reanalysis data sets. We first validated the winds in these analysis data sets by comparing them with WINDAS winds. MANAL and JRA25 perform best in reproducing the diurnal and semidiurnal wind components measured by WINDAS, including their horizontal distributions and seasonal variations.

Figure 18 summarizes the month–height distributions of the dynamical processes that primarily control the diurnal wind component over the main Japanese islands, as revealed by an analysis of WINDAS data (by SF10) and MANAL1 and JRA25 data (the present study). Local wind systems (e.g., land–sea breezes) prevail near the surface, and their return currents extend up to  $\sim 3$  km throughout most of the year. Below  $\sim 3$  km, DEEs prevail around Japan and influence the diurnal component. The DEEs exist throughout the year, but their influence on diurnal winds over the main Japanese islands is small in JJA. Above 3 km, local wind systems and DEEs have only a minor influence on the diurnal wind component. Medium-scale eastward-traveling waves with amplitude maxima in the upper troposphere make a large contribution to the diurnal wind component at 3–5 km in winter–spring. In contrast, the diurnal tide is predominant at 3–5 km in summer–autumn, although it exists over the entire lower troposphere throughout the year.

In the region equatorward of  $\sim 30^\circ\text{N}$ , including WINDAS stations located on small southern islands, the diurnal wind component is controlled primarily by the diurnal tide in the entire lower troposphere throughout the year.

Possible dynamical mechanisms for the DEEs are as follows. Yamamori et al. (1997) noted the existence of eastward-traveling waves below 700 hPa over the Northwestern Pacific, including Japan ( $10\text{--}70^\circ\text{N}$ ,  $80\text{--}180^\circ\text{E}$ ), with an average zonal phase speed of  $17\text{ m s}^{-1}$ . These characteristics are largely consistent with those of the DEEs reported in the present study; thus, the waves described by Yamamori et al. (1997) may be identical to the DEEs. Garreaud and Munoz (2004) studied a traveling phenomenon in the lower troposphere along the west coast of South America ( $15\text{--}25^\circ\text{S}$ ) with a phase velocity of  $30\text{ m s}^{-1}$ , although showing westward propagation. The authors suggested that this system was generated by local wind systems between the high mountainous region along the west coast of the continent and the adjacent ocean, and that the system was maintained as gravity waves. In the present study, we found that DEEs around Japan satisfy the geostrophic relationship; thus, they are not considered as gravity waves. Given that the medium-scale waves in the upper troposphere are considered to be maintained as neutral edge waves at the upper boundary in the Eady problem (e.g., Eady 1949; Tomikawa et al. 2006), the DEEs may correspond to neutral edge waves at the lower rigid boundary in the Eady problem. Theoretically, the lower edge waves are slower than the upper edge waves; this is qualitatively consistent with our finding that the DEEs are slower than medium-scale waves. In the Eady solutions, the zonal phase velocity and vertical scale of the lower edge waves are expressed as  $fU_z/Nk_h$  and  $f/Nk_h$ , respectively, where  $f$  is the Coriolis parameter,  $U_z$  is the vertical shear of the background winds,  $N$  is the Brunt–Vaisalla frequency, and  $k_h$  is the total horizontal wavenumber ( $\sqrt{k^2 + l^2}$ ) (e.g., chapter 6 in Vallis 2006). If we assume  $f = 1.0 \times 10^{-4}\text{ s}^{-1}$ ,  $U_z = 5\text{ s}^{-1}$ , and  $N = 1.0 \times 10^{-2}\text{ s}^{-1}$ , which are typical values in the midlatitude troposphere, and that  $k = l = 2\pi/1500\text{ km}^{-1} = 4.5 \times 10^{-6}\text{ m}^{-1}$ , which are values obtained for DEEs, then the theoretical zonal phase speed and vertical length scale become  $\sim 10\text{ m s}^{-1}$  and  $\sim 2\text{ km}$ , respectively, approximately consistent with the present findings. Therefore, DEEs are likely to be neutral edge waves in midlatitudes with

a vertical wind shear. Additional studies are required to identify the selection mechanisms of horizontal wavelength ( $\sim 1500\text{ km}$ ) or periodicity. It is also necessary to study the generation mechanisms and seasonal dependency of DEEs based on numerical simulations.

The present results demonstrate that global reanalysis data can be used to study the diurnal tide. Note that it is in the troposphere and stratosphere that the tides are excited; therefore, it is important to use reanalysis data to determine the excitation mechanism, global structure, and seasonality of such tides, in order to obtain a comprehensive understanding.

With regard to medium-scale waves in the upper troposphere, we confirmed the suggestion by Kodama et al. (2008) that the medium-scale waves contribute to the diurnal wind component, at least over East Asia. This finding may provide a key in understanding the generation mechanism of this phenomenon.

#### Acknowledgments

WINDAS data were provided by the Japan Meteorological Agency (JMA). JRA25/JCDAS data were provided by the cooperative research project of the JRA-25 long-term reanalysis by JMA and the Central Research Institute of Electric Power Industry (CRIEPI). ERA-Interim data were obtained from the ECMWF Data Server, and NCEP Reanalysis data were provided by NOAA/OAR/ESRL PSD, Boulder, Colorado, USA, accessed from their Web site at <http://www.cdc.noaa.gov/>. We wish to express our gratitude to Dr. Toshitaka Tsuda and Dr. Maura Hagan for helpful discussions regarding the diurnal tide, and to Dr. Atsushi Kubokawa for helpful discussions regarding the dynamical mechanisms of DEEs. We are also grateful to Dr. Isamu Hirota and two anonymous reviewers for their helpful comments and suggestions. This work was supported by the JGC-S Scholarship Foundation, and by the Japanese Ministry of Education, Culture, Sports, Science and Technology (MEXT) through Grants-in-Aid for Scientific Research (2200295800). Figures 1–17 were drawn using the GFD-DENNOU Library.

#### References

- Cai, X.-M., and D. G. Steyn, 2000: Modelling study of sea breezes in a complex coastal environment. *Atmos. Environ.*, **34**, 2873–2885.

- Eady, E. T., 1949: Long waves and cyclonic waves. *Tellus*, **1**, 33–52.
- Garreaud, R. D., and R. Munoz, 2004: The diurnal cycle in circulation and cloudiness over the subtropical southeast Pacific: A modeling study, *J. Clim.*, **17**, 1699–1710.
- Haurwitz, B., and A. D. Cowley, 1973: The diurnal and semidiurnal barometric oscillations, global distribution and annual variation. *Pure Appl. Geophys.*, **102**, 193–222.
- JMA Numerical Prediction Division, 2008: The JMA nonhydrostatic model II. *Report of Numerical Prediction Division* (in Japanese), **54**, JMA, 265 pp.
- Kalnay, E., M. Kanamitsu, R. Kistler, W. Collins, D. Deaven, L. Gandin, M. Iredell, S. Saha, G. White, J. Woollen, Y. Zhu, M. Chelliah, W. Ebisuzaki, W. Higgins, J. Janowiak, K. C. Mo, C. Ropelewski, J. Wang, A. Leetmaa, R. Reynolds, R. Jenne, and D. Joseph, 1996: The NCEP/NCAR 40-year reanalysis project. *Bull. Amer. Meteor. Soc.*, **77**, 437–471.
- Kanamitsu, M., W. Ebisuzaki, J. Woollen, S.-K. Yang, J. J. Hnilo, M. Fiorino, and G. L. Potter, 2002: NCEP-DOE AMIP-II reanalysis (R-2). *Bull. Amer. Meteor. Soc.*, **83**, 1631–1643.
- Kodama, Y.-M., K. Egawa, and M. Takahashi, 2008: Medium-scale tropopausal waves visualized by upper-level clouds to the east of Tibetan Plateau. *J. Meteor. Soc. Japan*, **86**, 279–295.
- Lieberman, R. S., and C. B. Leovy, 1995: A numerical model of nonmigrating diurnal tides between the surface and 65 km. *J. Atmos. Sci.*, **52**, 389–409.
- Nitis, T., D. Kitsiou, Z. B. Klaic, M. T. Prtenjak, and N. Moussiopoulos, 2005: The effects of basic flow and topography on the development of the sea breeze over a complex coastal environment. *Quart. J. Roy. Meteor. Soc.*, **131**, 305–327.
- Onogi, K., J. Tsutsui, H. Koide, M. Sakamoto, S. Kobayashi, H. Hatsushika, T. Matsumoto, N. Yamazaki, H. Kamahori, K. Takahashi, S. Kadokura, K. Wada, K. Kato, R. Oyama, T. Ose, N. Mannoji, and R. Taira, 2007: The JRA-25 reanalysis. *J. Meteor. Soc. Japan*, **85**, 369–432.
- Sakazaki, T., and M. Fujiwara, 2008: Diurnal variations in summertime surface wind upon Japanese plains: Hodograph rotation and its dynamics. *J. Meteor. Soc. Japan*, **86**, 787–803.
- Sakazaki, T., and M. Fujiwara, 2010: Diurnal variations in lower-tropospheric wind over Japan. Part I: Observational results using the Wind Profiler Network and Data Acquisition System (WINDAS). *J. Meteor. Soc. Japan*, **88**, 325–347.
- Sato, K., H. Eito, and I. Hirota, 1993: Medium-scale travelling waves in the extra-tropical upper troposphere. *J. Meteor. Soc. Japan*, **71**, 427–436.
- Simmons, A. J., S. M. Uppala, D. Dee, and S. Kobayashi, 2006: ERA-Interim: New ECMWF reanalysis product from 1989 onwards. *ECMWF Newsl.*, **110**, 25–35.
- Tijm, A. B. C., A. A. N. Holtslag, and A. J. van Delden, 1999: Observations and modeling of the sea breeze with the return current. *Mon. Wea. Rev.*, **127**, 625–640.
- Tsuda, T., and S. Kato, 1989: Diurnal non-migrating tides excited by a differential heating due to land-sea distribution. *J. Meteor. Soc. Japan*, **67**, 43–55.
- Uppala, S. M., D. Dee, S. Kobayashi, P. Berrisford, and A. J. Simmons, 2008: Towards a climate data assimilation system: Status update of ERA-Interim. *ECMWF Newsl.*, **115**, 12–18.
- Vallis, G. K., 2006: *Atmospheric and oceanic fluid dynamics*, Cambridge University Press, 745pp.
- Willmott, C. J., 1982: Some comments on the evaluation of model performance. *Bull. Amer. Meteorol. Soc.*, **63**, 1309–1313.
- Yamamori, M., K. Sato, and I. Hirota, 1997: A study on seasonal variation of upper tropospheric medium-scale waves over East Asia based on regional climate model data. *J. Meteor. Soc. Japan*, **75**, 13–22.